

Electronic structure of the ternary chalcopyrite semiconductors CuAlS₂, CuGaS₂, CuInS₂, CuAlSe₂, CuGaSe₂, and CuInSe₂

J. E. Jaffe and Alex Zunger

Solar Energy Research Institute, Golden, Colorado 80401

and Department of Physics, University of Colorado, Boulder, Colorado 80309

(Received 31 May 1983)

The electronic structure of six Cu-based ternary chalcopyrite semiconductors is calculated self-consistently for the first time within the density-functional formalism. The chemical trends in the band structures, electronic charge densities, density of states, and chemical bonding are analyzed.

I. INTRODUCTION

There are two major groups of ternary ABX_2 semiconductors. Group I (ternary chalcopyrites) consists of the $A^I B^{III} X_2^{VI}$ compounds where $A = \text{Cu, Ag}$; $B = \text{Al, Ga, In, Tl}$; and $X = \text{S, Se, Te}$. It is an isoelectronic analog of the II-VI binary compound semiconductors. Group II (ternary pnictides) consists of the $A^{II} B^{IV} X_2^V$ compounds, where $A = \text{Zn, Cd}$; $B = \text{Si, Ge, Sn}$; and $X = \text{P, As, Sb}$. It is an isoelectronic analog of the III-V binary compound semiconductors. The crystal structure of the ternary chalcopyrites (Fig. 1) belongs to nonsymmorphic space group D_{2d}^{12} (eight atoms per primitive unit cell), which is a superlattice of zinc-blende structure T_d^2 (two atoms per primitive unit cell). Each anion is coordinated by two A and two B cations, whereas each cation is tetrahedrally coordinated by four anions. There are three significant structural differences with respect to the zinc-blende structure. First, there are two cation sublattices rather than one, leading to the existence of two basic near-neighbor chemical bonds $A-X$ and $B-X$, with generally unequal bond lengths

$R_{AX} \neq R_{BX}$. Second, the unit cell is tetragonally distorted with a distortion parameter $\eta \equiv c/2a \neq 1$. Third, the anions are displaced from the ideal tetrahedral site by an amount u . The two near-neighbor bond distances are given by $R_{AX} = a[u^2 + (1 + \eta^2)/16]^{1/2}$ and $R_{BX} = a[(u - \frac{1}{2})^2 + (1 + \eta^2)/16]^{1/2}$, where a is the cubic lattice constant. The bond length mismatch is hence $\alpha \equiv R_{BX}^2 - R_{AX}^2 = (u - \frac{1}{4})a^2$ and vanishes for a zinc-blende-like undistorted anion sublattice, where $u \equiv \frac{1}{4}$. Because of the added structural (η, u) and chemical ($A \neq B$) degrees of freedom relative to their binary analogs, the 36 known ternary ABX_2 semiconductors exhibit a far richer range of physical and chemical properties. These were discussed in a number of recent review articles¹⁻⁸ as well as in four conference proceedings.⁹⁻¹² The broad range of optical band gaps and carrier mobilities offered by ternary ABX_2 semiconductors, as well as their ability to form various solid solutions and to accommodate different dopants, has recently led to their emergence as technologically significant device materials, including applications in photovoltaic solar cells both as single-crystal materials (up to 12% efficient^{13,14}) and as polycrystalline thin films (at least 9.4% efficient¹⁵), light-emitting diodes,¹⁶ and in various nonlinear optical devices.⁸ This paper is concerned with the calculation of the electronic structure of group-I ternary chalcopyrite semiconductors. A planned future paper¹⁷ will discuss the properties of group-II ternary pnictides.

Despite the unusual richness in interesting physical phenomena in group-I chalcopyrites, the extensive progress made in experimental studies¹⁻¹² of these materials has not been matched by theoretical studies. Among the factors contributing to this situation we note several considerations: (i) The structural complexity of the chalcopyrite unit cell (eight atoms per cell with low site symmetries) makes the electronic structure calculation considerably more difficult than for binary zinc-blende semiconductors. (ii) The unambiguous evidence³ for the participation of the noble-atom d orbitals in bonding through hybridization with the anion sp states implies that *local* pseudopotential approximations (which ignore the $A^I d$ orbitals), used successfully to describe sp^3 -bonded binary semiconductors,¹⁸ are insufficient for group-I ternary semiconductors. (iii) If one were to use *nonlocal* pseudopotentials,

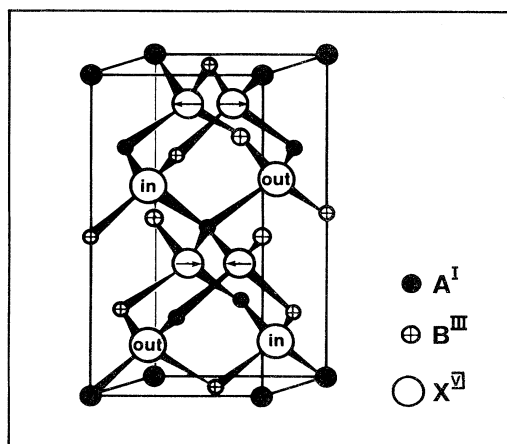


FIG. 1. Crystal structure of the chalcopyrite ABX_2 unit cell. The arrows and the denoted in-plane and out-of-plane directions show the anion displacements relative to the tetrahedral structure.

tials,¹⁹ in a conventional plane-wave basis set the problem of obtaining a converged expansion in basis functions would be intractable. This is so because there are no d states in the core of the Cu atom, hence its d nonlocal pseudopotential is purely Coulombic,¹⁹ requiring $\sim 10^3$ – 10^4 plane-wave basis functions. In a mixed-basis representation, much fewer basis functions are needed (see below). Whereas the former limit is unattainable, current methods of matrix diagonalization (e.g., Householder-Choleski methods) make even the latter limit a formidable computational task. (iv) The lack of precise assignment of the few lowest optical band gaps to well-defined interband transitions restricts the use of empirical fitting of the band structure,¹⁸ as done successfully for binary systems. (v) Accumulating evidence for the polarity of the bonds^{1–6} suggests that self-consistent calculations (which describe charge transfer) are needed. Attaining self-consistency in the presence of localized orbitals (e.g., $A^1 d$ states and the $X^{VI} s$ states) that coexist in a similar energy range with itinerantly delocalized orbitals (e.g., the $X^{VI} p$ states) can be a formidable computational task, using current computational techniques (various forms of diagonal mixing).

There were three previous attempts to calculate the electronic structure of group-I chalcopyrites. Poplavnoi *et al.*^{20,21} have used the non-self-consistent empirical pseudopotential method,¹⁸ neglecting the noble-atom d orbitals. The pseudopotential form factors of the B and X atoms were taken from the II-VI binary analogs, whereas the form factors of Cu were taken from early results of Harrison.²² The band structure was evaluated at four high-symmetry \vec{k} points, using a maximum of 150 plane waves. While early calculations²⁰ ignored the anion displacement (leading to *indirect* band gaps, in contrast with experiment³), more recent calculations²¹ included this effect ($u \neq \frac{1}{4}$). Results were obtained²¹ for CuAlS₂, CuInS₂, CuAlSe₂, and CuInSe₂. More recently, Oguchi *et al.*²³ have applied the self-consistent numerical linear combination of atomic orbitals (LCAO) approach of Zunger and Freeman²⁴ to study the band structure of CuAlS₂ and CuGaS₂. The original method²⁴ was simplified by neglecting all nonspherical contributions to the charge density and by using a small basis set. No convergence tests were reported. In Sec. VI, we will compare the results of the present study with the results of Refs. 21 and 23. Finally, Bendt and Zunger²⁵ have recently reported the results of a first self-consistent study of the electronic structure of CuInSe₂. They used the recently developed potential-variation mixed-basis (PVMB) approach, which avoids pseudopotential approximations and solves the all-electron problem self-consistently within the density-functional approach.²⁶

In the present paper we use the PVMB approach to study the chemical trends in the electronic structure of CuAlS₂, CuGaS₂, CuInS₂, CuAlSe₂, CuGaSe₂, and CuInSe₂. The PVMB method overcomes the difficulties (enumerated above) posed by the previous computational techniques by using a number of new approaches to the problem. These are briefly summarized in Sec. II. We note, however, at the outset that since we are using the density-functional approach²⁶ to describe the interelec-

tronic interactions in the system, the one-electron excitation energies and one-electron removal energies are not guaranteed to be correctly described, for reasons discussed previously in detail.^{27,28} In fact, all optical band gaps of the CuBX₂ semiconductors are found to be 1–1.5 eV too small relative to experiment. While the discrepancy could be removed by a simple empirical adjustment, as shown in Sec. IX, the need for such an *ad hoc* adjustment reflects our present ignorance of the details of interelectronic correlations in inhomogeneous electron systems. Our outlook for the present work is therefore as follows. We will use the state-of-the-art theoretical technology offered by the PVMB method to solve very precisely for the electronic structure of six chalcopyrite crystals within the local-density-functional formalism.²⁶ We will use the most recent description of the local-density interelectronic correlation functional due to Ceperley and Alder²⁹ [calculated in close form in Ref. 27(c)], which constitutes a nearly-exact solution for the homogeneous electron gas. The sophistication of the computational technique allows us to come close to local-density limit in the sense that internal computational approximations are largely eliminated and hence the results reflect the predictions of the underlying local-density theoretical framework^{26,29} to within a precision of 0.1–0.2 eV for the band-structure energies in a region of ± 10 eV around the Fermi energy E_F and ~ 1 – 2% in the charge density. Using this first-principles approach, we will attempt the first theoretical systematic description of the chemical trends in the electronic structure of six group-I chalcopyrite semiconductors. We are particularly interested in examining the trends in (i) the electronic band structure and its interpretation in terms of chemical bonds, (ii) the densities of states and their relation to x-ray photoemission data, (iii) the ground-state electronic charge densities and their significance in elucidating the chemical bonding in the system, (iv) the role played by the noble-atom d orbitals, and (v) the way that the structural anomalies (relative to the zinc-blende binary compounds) control the electronic structure. Having obtained a coherent description of the chemical trends in this series with a theoretically well-defined (but imperfect) correlation functional,²⁹ we will show how the major deficiency of this description (small band gaps) can be empirically alleviated by adjusting a single parameter. We will comment upon the extent to which the empirically adjusted results affect our understanding of the chemical trends obtained before.

II. THEORETICAL APPROACH

We use the PVMB method described in detail previously.²⁵ The major characteristics of the method are as follows: (1) It avoids any pseudopotential approximations, i.e., it constitutes an all-electron approach. Hyperdeep core orbitals are selectively frozen if this approximation is found to result in an error in the valence and conduction bands of less than ~ 0.1 eV. (2) No shape approximation (muffin-tin or other) is applied to the potential or the charge density. (3) The mixed-basis set used consists of a combination of numerical, coordinate-space compressed atom orbitals (which accurately describe the rapid wave-

function variations near the nuclei) plus a set of symmetrized plane-wave basis functions (which describe the weaker spatial variations in the interstitial regions). All multicentered integrals are eliminated by using nonoverlapping compressed atom orbitals. Basis orbitals are added until the error in the band energies in the region of $E_F \pm 10$ eV is below ~ 0.1 eV. (4) The crystal potential is described²⁴ as a sum of a fixed, multicenter term (superposition of renormalized quasi-atom-potentials²⁵) and a Fourier series with adjustable coefficients $\mu_{\vec{G}}$, which describe all nonspherical terms. Rather than use the conventional variational approach (minimize the total energy with respect to the orbitals), we use an equivalent but computationally far more efficient potential-variation approach²⁵ (minimize the total energy with respect to the potential-variational parameters $\mu_{\vec{G}}$). The number of such Fourier coefficients is increased until the error is reduced below our prescribed tolerance. (5) The Hamiltonian matrix elements are computed within the prescribed set of the basis orbitals and the crystal potential, essentially with no approximations except for convergence parameters. These are increased to attain the prescribed precision tolerance. (6) Standard (Hausholder-Choleski) matrix diagonalization methods are ineffective for large ($N \cong 10^3 \times 10^3$) and general Hermitian Hamiltonian matrices, particularly if only a smaller number ($M \cong 50$) of lowest eigenvectors are needed. We use the residual minimization method³⁰ (RMM) to dramatically simplify this problem. It requires the diagonalization of only a small submatrix (approximately 100×100) by standard methods and then uses an iterative technique, analogous to a high- (e.g., seventh-) order perturbation theory to include the effect of all other matrix elements to obtain eigenvectors to an arbitrary precision. The method is much faster than standard diagonalization algorithms if $M < N$, does not require storing the $N \times N$ matrix, and is far more accurate than standard low-order perturbation techniques, such as Löwdin's method.³¹ (7) Self-consistency is attained by using a Newton-Raphson Jacobian-update method.²⁵ This method does not require any new information beyond that already available from the band-structure calculation, as it "remembers" information from all past iterations and is able to use this information effectively in constructing the best guess for the next iteration, without human intervention. It enables us to obtain self-consistent solutions very rapidly even in the presence of nonlinearities, in contrast to other approaches.³²

Convergence tests for this method were described previously in detail²⁵ and will not be repeated here. To monitor the error due to truncation of the basis-set expansions we have compared the self-consistent band structure of CuAlS₂ calculated with a "standard setting" of 570 basis functions at point Γ (58 coordinate space orbitals plus 512 symmetrized plane waves) with a highly converged (about ± 0.01 eV) calculation, using 852 basis functions at point Γ . Relative to the "standard" calculation, the highly converged calculation shows a lowering of the upper valence bands (at $\epsilon \leq E_{\text{VBM}} - 5$ eV) by less than or equal to 0.12 eV, a lowering of the $B^{\text{III}}-X^{\text{VI}}$ bands (at $\epsilon \leq E_{\text{VBM}} - 7$ eV) by less than or equal to 0.06 eV, and an upward shift of

TABLE I. Values of the cubic lattice constant a , the tetragonal distortion parameter $\eta \equiv c/2a$, and the anion displacement parameter u (in units of a) used in the present calculation (Ref. 33). We use 1 a.u. = 0.529 17 Å.

Compound	a (a.u.)	η	u
CuAlS ₂	10.0800	0.979	0.275
CuGaS ₂	10.1216	0.974	0.275
CuInS ₂	10.4372	1.0065	0.214
CuAlSe ₂	10.5864	0.977	0.269
CuGaSe ₂	10.6091	0.9825	0.250
CuInSe ₂	10.9303	1.004	0.224

the X^{VI} s band (at $\epsilon \leq E_{\text{VBM}} - 15$ eV) by less than 0.4 eV. This deep band is therefore the most sensitive one, and the results obtained for it with the "standard setting" may reflect an overestimate. The lowest five conduction bands are lowered by only less than 0.05 eV. The x-ray scattering factors and ground-state charge density are found to change by less than 1%.

The compressed atom radii²⁵ used for Cu, Al, Ga, In, S, and Se are 2.9, 2.7, 2.9, 3.2, 2.7, and 2.9 a.u., respectively, and the quasi atom radii²⁵ for the same elements are taken as the Pauling tetrahedral radii 2.6, 2.4, 2.4, 2.9, 2.0, and 2.2 a.u., respectively. The crystal-structure parameters used are taken from Ref. 33 and are given in Table I. The coordinates of the atoms are given in Table II. Self-consistency is obtained to within a tolerance of ~ 1 mRy, by sampling the charge density at a single special \vec{k} point³⁴ $\vec{k} = (2\pi/a)(\frac{1}{4}, \frac{1}{4}, \frac{1}{4})$. The band structure was calculated at 13 \vec{k} points along the $T-\Gamma-N$ lines. To connect the various bands through \vec{k} space we calculate the overlap of the eigenstates $\psi_i(\vec{k}_1, \vec{r})$ and $\psi_j(\vec{k}_2, \vec{r})$ at successive \vec{k} points \vec{k}_1 and \vec{k}_2 with a phase factor included:

$$S_{ij}(\vec{k}_1, \vec{k}_2) = \int d^3\vec{r} e^{i(\vec{k}_1 - \vec{k}_2) \cdot \vec{r}} \psi_i^*(\vec{k}_1, \vec{r}) \psi_j(\vec{k}_2, \vec{r}).$$

The overlap element $S_{ij}(\vec{k}_1, \vec{k}_2)$ should be of order unity for two eigenvalues that belong to the same band and should be small when they belong to different bands. Al-

TABLE II. Coordinates of the eight atoms in the chalcopyrite ABX_2 unit cell. The lattice vectors are $a_1 = a(1, 0, 0)$, $a_2 = a(0, 1, 0)$ and $a_3 = a(\frac{1}{2}, \frac{1}{2}, \eta)$. The unit cell volume is $a^2c/2$.

Atom	Coordinates
A_1	0, 0, 0
A_2	0, $a/2$, $c/4$
B_1	$a/2$, $a/2$, 0
B_2	$a/2$, 0, $c/4$
X_1	$a(\frac{1}{4} + u)$, $a/4$, $c/8$
X_2	$a(\frac{3}{4} - u)$, $3a/4$, $c/8$
X_3	$a/4$, $a(\frac{3}{4} + u)$, $3c/8$
X_4	$3a/4$, $a(\frac{1}{4} - u)$, $3c/8$

though this automatic procedure is not error proof near multiple band crossing points, we find that it gives the correct band connectivities about 95% of the time, and most erroneous connections can be corrected on the basis of symmetry considerations. After noting the connections of successive points by line segments, we have fitted the bands with smooth curves whose derivatives show the proper behavior as they approach Γ , T , and N . Density-of-state diagrams were computed from 18 special \vec{k} points (and hence only coarse histograms with a channel width of 0.2 eV are given), and charge-density plots were generated from a six special \vec{k} -point sampling.

III. BAND STRUCTURES

Figures 2–4 display the self-consistent electronic band structures of six $A^I B^{III} X_2^{VI}$ compounds for $A^I = \text{Cu}$, $B^{III} = \text{Al, Ga, In}$, and $X^{VI} = \text{S, Se}$, calculated with Ceperley's correlation^{27(c),29} and the crystal-structure parameters of

Table I. Because of the complexity of the band structures, we show in Fig. 5 a simplified generic band structure of a $A^I B^{III} X_2^{VI}$ compound, establishing the important subbands (shaded areas) and the terminology for the significant critical points. We will examine the chemical nature of the various states by calculating the electronic charge densities in energy slices corresponding to these subbands. We use the notation of Refs. 20 and 21 to label the bands with the addition that states with identical labels (e.g., N_1, T_5) are given additional superscripts in increasing order of energy (e.g., $N_{1v}^{(1)}, N_{1v}^{(2)}$, etc.). We will use Fig. 5 to discuss the overall features of the band structures. Table III provides the energies of all valence-band critical points in the notation of Fig. 5. The zero of energy is set at the $\Gamma_{4v}^{(2)}$ valence-band maximum (VBM). Figure 5 shows that for all six materials there are four distinct valence-band regions between the valence-band maximum and $\sim E_{\text{VBM}} - 18$ eV, separated by three "heteropolar gaps" (boxed numbers in Fig. 5). We discuss the various subbands in order of increasing binding energy.

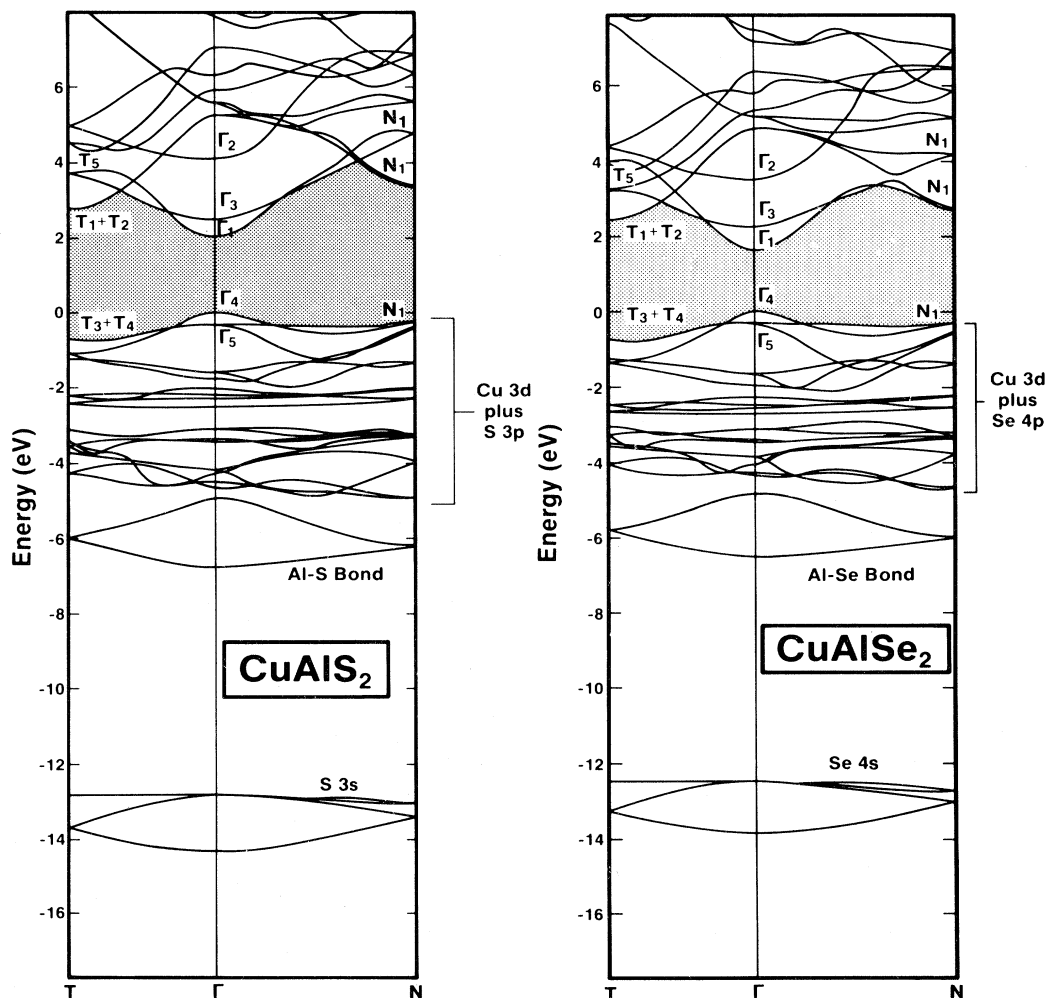


FIG. 2. Electronic band structure of CuAlS₂ and CuAlSe₂ using Ceperley's correlation and the crystal-structure parameters of Table I. The principle band gap is denoted by the shaded areas.

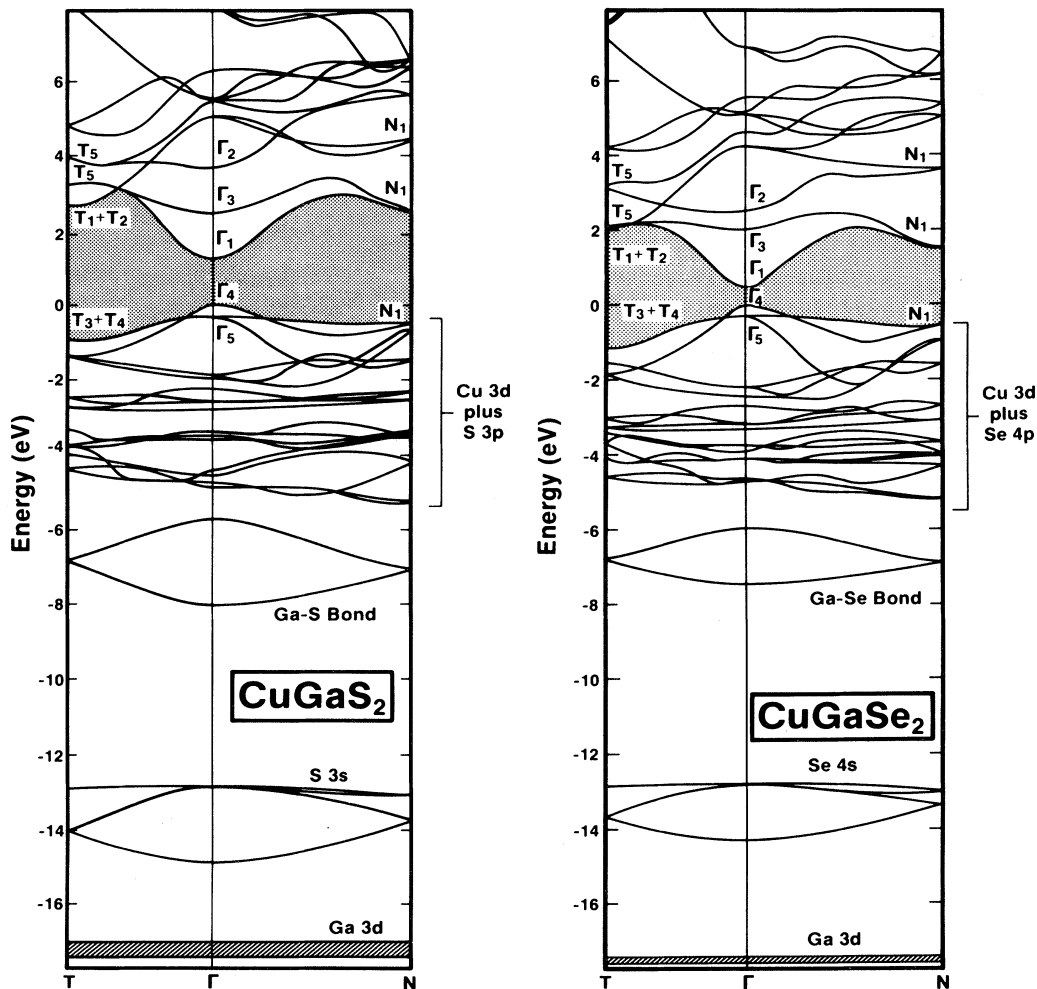


FIG. 3. Electronic band structure of CuGaS_2 and CuGaSe_2 using Ceperley's correlation and the crystal-structure parameters of Table I. The principle band gap is denoted by the shaded areas.

A. The upper valence band

1. Bands

The upper valence band has its maximum at the $\Gamma_{4v}^{(2)}$ point in the zone center; the conduction-band minimum is at the Γ_{1c} point, hence all six materials have a direct band gap. There are two secondary maxima in the upper valence band within ~ 1 eV of the VBM, located at $N_{1v}^{(5)}$ and $T_{3v} + T_{4v}$, with the former being always closer to the VBM than the latter. The minimum of the upper valence band always occur at or near the $N_{1v}^{(4)}$ point, with secondary minima at $\Gamma_{4v}^{(1)}$ and $T_{4v} + T_{5v}$. At the center of the Brillouin zone near the VBM we find the crystal-field-split pair $\Gamma_{4v}^{(1)}$ (singly degenerate) and $\Gamma_{5v}^{(2)}$ (doubly degenerate). With the use of the sign convention of Ref. 3, the crystal-field (CF) splitting between them is given by $\Delta_{CF} = \epsilon(\Gamma_{5v}^{(2)}) - \epsilon(\Gamma_{4v}^{(1)})$. It represents the effects of the (i) existence of two distinct cations $A \neq B$, (ii) tetragonal distortion $\eta \neq 1$, and (iii) anion displacement $u \neq \frac{1}{4}$. In the zinc-blende structure ($A = B$, $\eta = 1$, $u = \frac{1}{4}$) one has

$\Delta_{CF} \equiv 0$, and the $\Gamma_{4v}^{(2)} + \Gamma_{5v}^{(2)}$ pair forms the triply degenerate Γ_{25v} state at the VBM. Any of the three factors (i)–(iii) can lead to $\Delta_{CF} \neq 0$. We find, however, that the six chalcopyrite compounds fall into two distinct groups according to the magnitude of Δ_{CF} : Whereas CuInS_2 and CuInSe_2 have a small tetragonal distortion $\eta = 1.004\text{--}1.0065$ (Table I) and show a very small Δ_{CF} , the remaining four materials have a noticeable tetragonal compression ($\eta < 1$, cf. Table I), and all show $\Delta_{CF} < 0$ in the neighborhood of ~ -0.3 eV. This suggests that factor (ii) above is the decisive one. Notice, however that for the Cu-based ternary chalcopyrites, the crystal-field splitting Δ_{CF} does not scale linearly with $\eta - 1$ [i.e., Δ_{CF} is not given by $b(\eta - 1)$], as found for group-II chalcopyrites.³ In general, the $\Gamma_{5v}^{(2)}$ state is split by the spin-orbit interaction (neglected in the present work) into the $\Gamma_{6v} + \Gamma_{7v}$ components.

The width of the upper valence band is given by $W_1 = \epsilon(\Gamma_{4v}^{(2)}) - \epsilon(N_{1v}^{(4)})$. It is seen (Table III) that W_1 for the sulfides is always larger than for the selenides and that the aluminum compounds always have the narrowest W_1 .

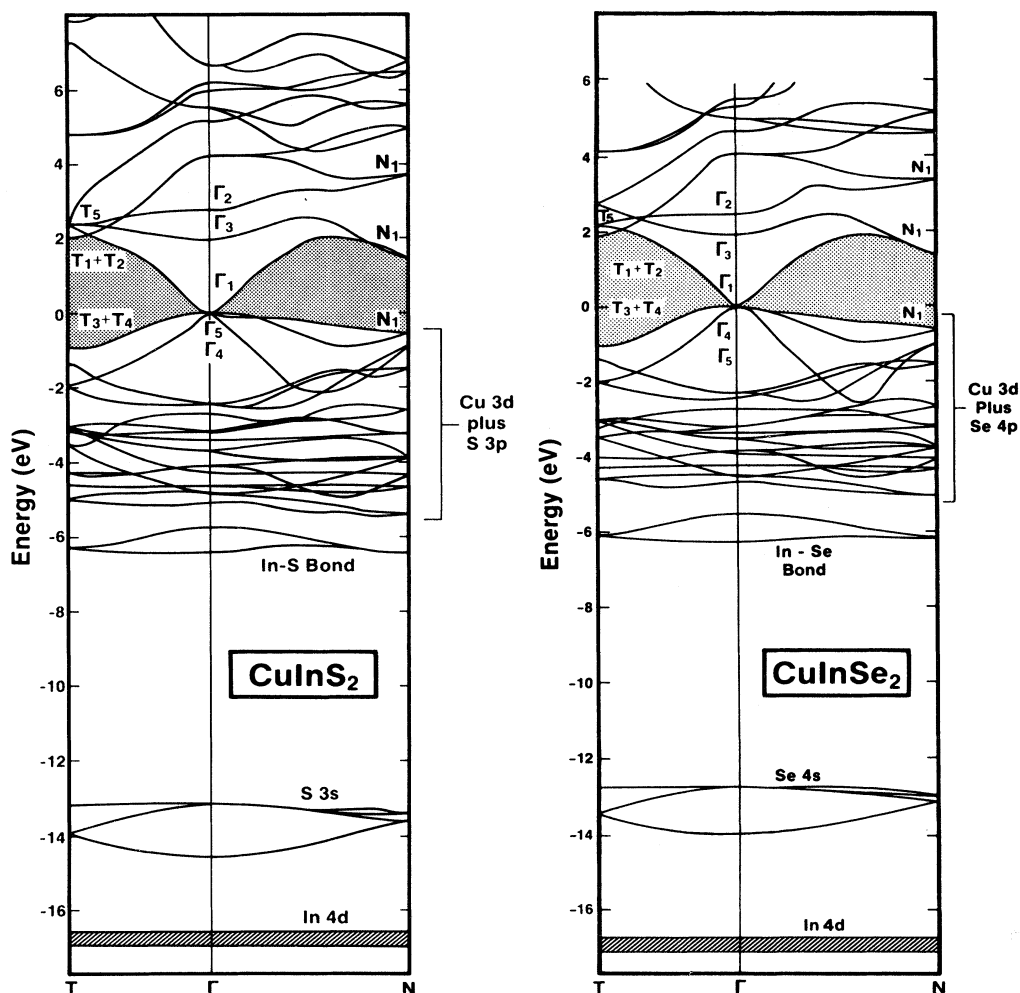


FIG. 4. Electronic band structure of CuInS₂ and CuInSe₂ using Ceperley's correlation and the crystal-structure parameters of Table I. The principle band gap is denoted by the shaded areas.

2. Electronic charge density

Figure 6 depicts the electronic charge density of the upper valence bands of the six group-I chalcopyrites. It is seen that the A^I-X^{VI} contact appears covalently bonded (cf. the "peanut-shaped" outer Cu- X contours) with a significant ionic component (i.e., the maximum of charge drawn closer to the X^{VI} site), whereas the $B^{III}-X^{VI}$ contact appears to be "nonbonding": The B^{III} atom merely fills up the space without forming a strong bond with the chalcogen atom. The Cu atom is seen to contribute significantly to the charge in the upper valence band. In fact, partial-wave analysis shows that it is the Cu d^{10} orbital, not its s orbital that makes up most of this charge. This is understandable in terms of simple chemical considerations: The orbital energy of the Cu $4s$ state (Hartree-Fock value^{35(a)} -6.5 eV, experimental^{35(b)} -7.7 eV) is considerably less negative than that of the chalcogen valence s states (Hartree-Fock values^{35(a)} of -23.9 and -22.8 eV,

and experimental values^{35(b)} of -20.2 and -20.15 eV, for S and Se, respectively). Hence, the occupied bonding combination (the X^{VI} band of Fig. 5) is made predominantly from the chalcogen orbitals whereas the Cu s character is repelled upwards outside of the valence band, into the conduction bands.

3. d character

The energy dependence of the Cu d character in the upper valence band can be appreciated from Fig. 7, which shows the Cu-centered d contribution to the (local) density of states. It is seen that the Cu d character reaches its maximum at 3–4 eV below the VBM, has a double-structure peak (resembling the e_g-t_g structure in the band structure of cubic elemental transition metals), and that the distance between its maximum and the VBM increases in the sequence Al \rightarrow Ga \rightarrow In. Clearly, the electronic structure of the upper valence band is dominated by the

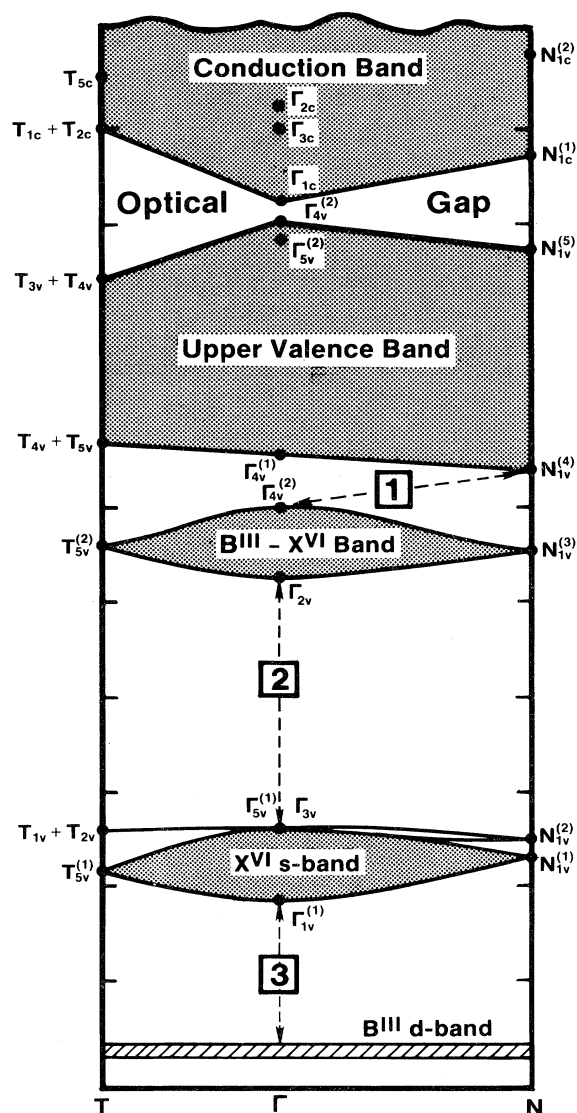


FIG. 5. Generic band diagram for a group-I ABX_2 chalcopyrite, establishing the notation used in the text and in Table III. Shaded and cross-hatched areas denote the major subbands, and boxed numbers indicate the three internal gaps.

$Cu d-Xp$ interactions, with the strongest interaction for the aluminum compound. This is the most significant difference between the structure of the upper valence bands of binary and ternary semiconductors.³⁶ This $Cu d$ character was ignored in previous pseudopotential calculations.^{20,21} We see that almost all of the $Cu d$ character is concentrated in the upper valence band, with only negligible amounts in the conduction band. We have noticed before that most of the $Cu s$ states are pushed from the valence bands into the conduction bands. Clearly, therefore, the Cu ion appears in $CuBX_2$ chalcopyrites as a monovalent cation³⁷ ($\sim d^{10}s^0$) and not as a divalent species ($\sim d^9s^0$) as in many of its inorganic complexes (e.g., CuO). This agrees with the recent results of Folmer³⁷ and Mirovsky,³⁸ showing that whereas the binding

energy determined in x-ray photoemission (XPS) experiments for the $In 3d$ states in $CuInS_2$ and $CuInSe_2$ is very close to the value for trivalent In compounds (In_2O_3 , In_2S_3), the binding energy of $Cu 2p$ in the ternary chalcopyrites is close to the value of monovalent Cu compounds (Cu_2S , Cu_2O) but is significantly lower than the value for divalent Cu compounds (CuO), suggesting the predominance of the monovalent form in the Cu chalcopyrites. Interestingly, $CuBX_2$ compounds exist for $X=S, Se, Te$ but not for $X=O$. It is likely that due to its larger electronegativity, the ternary oxide will have a *divalent* Cu cation and hence will be stabilized in a different crystal structure, and not in a chalcopyrite structure. Indeed, the copper indium oxide $Cu_2In_2O_5$ is orthorhombic.

The existence of $Cu d$ character in the upper valence band has a significant consequence for the optical band gaps in these materials.³⁶ The $\Gamma_{15}(d)$ -like combinations of the d orbitals interact with the $\Gamma_{15}(p)$ -like combinations of the anion p orbitals ($\Gamma_{4v}^{(7)} + \Gamma_{5v}^{(2)}$) at the VBM. The strength of this interaction depends inversely on the energy separation between the $Cu d$ orbitals and the anion p orbitals: It is expected hence to be stronger for the sulfides than for the selenides.³⁵ This repulsive interaction pushes the higher energy component [$\Gamma_{15}(p)$ -like] to higher energies, reducing thereby the band gap relative to systems with more tightly bound d orbitals (e.g., Zn - or Cd -based binaries). We have previously found³⁶ that this $p-d$ repulsion accounts for about half of the observed reduction in the band gaps of the $CuBX_2$ compounds relative to their II-VI binary analogs. Notice that the proximity ($\sim 1-2$ eV) of the atomic $Cu d$ orbitals to the atomic chalcogen p orbitals³⁵ immediately suggests that the former cannot be discarded from the spectrum by using local-pseudopotential approximations.^{20,21} The massive participation of the $Cu d$ orbitals in bonding in the upper valence bands of $CuBX_2$ compounds (Figs. 6 and 7) is made possible by this orbital energy proximity. As one replaces Cu by Ag , Zn , or Cd , this $d-p$ atomic energy gap increases rapidly,³⁵ leading to a reduction in $d-p$ hybridization and to the predominance of sp bonding. Indeed, such binary analogs ($ZnSe$, $CdSe$, etc.) are known to be unstable towards photoelectrochemical reduction by optically generated holes, leading to the breaking of the cation-anion bonds and to precipitation of the anion in its elemental form.³⁸ The foregoing discussion suggests that the participation of the $Cu d$ orbitals in bonding in $CuBX_2$ compounds (*viz.*, the covalent $Cu-X$ contacts in Fig. 6) may account for their extraordinary stability against breaking the $Cu-X$ bonds: In $CuBX_2$ a photoelectron is removed from a band that is antibonding with respect to $d-p$ interactions, therefore, although one breaks a $s-p$ bond, at the same time a $d-p$ bond is created.

Shay and Kasper³⁹ (see also Ref. 3, p. 118) have attempted to extract the fractional d character α_d of the top of the valence bands of ternary chalcopyrites by assuming that the observed spin-orbit splitting is given as a weighted average of the spin-orbit splitting in the (p -like) binary analog and the splitting of the d levels of the ternary compounds. From this analysis they suggested that $CuInSe_2$,

TABLE III. Calculated valence-band energies at high symmetry points (in eV), given relative to the $\Gamma_{4v}^{(2)}$ valence-band maximum. Notation refers to Fig. 5. The Ceperley correlation [Refs. 27(c) and 29] and the crystal-structure parameters of Table I are used.

State	Compound					
	CuAlS ₂	CuGaS ₂	CuInS ₂	CuAlSe ₂	CuGaSe ₂	CuInSe ₂
Upper VB						
Maxima						
$\Gamma_{4v}^{(2)}$	0.0	0.0	0.0	0.0	0.0	0.0
$\Gamma_{5v} = \Delta_{CF}$	-0.32	-0.32	0.075	-0.30	-0.34	-0.03
$T_{3v} + T_{4v}$	-0.67	-0.91	-0.91	-0.76	-1.14	-1.05
$N_{1v}^{(5)}$	-0.24	-0.48	-0.54	-0.30	-0.58	-0.63
Minima						
$\Gamma_{4v}^{(1)}$	-4.63	-4.85	-5.07	-4.32	-4.74	-4.66
$T_{4v} + T_{5v}$	-4.24	-4.37	-4.90	-4.08	-4.61	-4.64
$N_{1v}^{(4)}$	-4.92	-5.26	-5.41	-4.69	-5.21	-5.02
$B^{III}-X^{VI}$ band						
$\Gamma_{1v}^{(2)}$	-4.93	-5.71	-5.73	-4.86	-6.01	-5.52
Γ_{2v}	-6.74	-8.00	-6.40	-6.51	-7.50	-6.32
$T_{5v}^{(2)}$	-5.99	-6.82	-6.29	-5.81	-6.80	-6.15
$N_{1v}^{(3)}$	-6.21	-7.07	-6.41	-5.99	-6.92	-6.17
X^{VI} s band						
$\Gamma_{5v}^{(1)}$	-12.81	-12.85	-13.15	-12.49	-12.81	-12.75
Γ_{3v}	-12.83	-12.89	-13.18	-12.49	-12.78	-12.75
$\Gamma_{1v}^{(1)}$	-14.32	-14.87	-14.57	-13.83	-14.32	-14.00
$T_{1v} + T_{2v}$	-12.82	-12.88	-13.18	-12.50	-12.82	-12.92
$T_{5v}^{(1)}$	-13.67	-14.03	-13.92	-13.23	-13.65	-13.58
$N_{1v}^{(2)}$	-13.05	-13.08	-13.41	-12.70	-13.04	-12.96
$N_{1v}^{(1)}$	-13.42	-13.77	-13.62	-13.01	-13.40	-13.18
B^{III} d band						
Center at point Γ		-17.2	-16.77		-17.5	-16.93
Width		0.38	0.37		0.18	0.43

CuGaSe₂, CuGaS₂, and CuAlS₂ have about the same percent d character (α_d values of 34%, 36%, 35%, and 35%, respectively), whereas CuInS₂ has a significantly higher d character of 45%. They have further suggested that the decrease ΔE_g in the band gaps of the ternary compounds relative to the binary analogs results exclusively from the existence of d character in the former compounds, as suggested to the authors by the linearity of the phenomenological relation $\Delta E_g = 3.125\alpha_d$, which they have deduced. However, the observed band-gap reduction $\Delta E_g \cong 2.4$ eV for CuAlS₂ (not shown in their³⁹ ΔE_g vs α_d plot) would imply $\alpha_d = 77\%$, considerably higher than their value of 35% inferred from their spin-orbit data. We suggest that this inconsistency results from the fact that the band-gap anomaly ΔE_g results both from the existence of d character (yielding a contribution ΔE_g^d to ΔE_g) and from a structural (S) anomaly ($u \neq \frac{1}{4}$) in the ternary chalcopyrites³⁶ (producing a contribution ΔE_g^S to ΔE_g). Only ΔE_g^d is expected to scale with the d character. We calculate directly the percent d character at the top of the valence band by decomposing the wave functions into angular momentum components and evaluating the fraction of d charge enclosed in a sphere of Pauling's radius. We find

for CuInSe₂, CuInS₂, CuGaSe₂, CuAlSe₂, CuGaS₂, and CuAlS₂, respectively, values of 22%, 24%, 26.6%, 27.5%, 31.5%, and 35.2% d character. In contrast to the Shay-Kasper values, these scale linearly³⁶ with the d -orbital-induced part of the band-gap anomaly ΔE_g^d . Our results hence indicate that CuAlS₂ has the highest d character in this series and that CuInSe₂ and CuInS₂ have the lowest d character, in contrast with the suggestion of Shay and Kasper³⁹ that CuInS₂ has the highest d character.

B. The $B^{III}-X^{VI}$ band

The upper valence band is separated by a small heteropolar gap (denoted as "gap 1" in Fig. 5) from the lower-lying valence band which we denote as the $B^{III}-X^{VI}$ band. This first heteropolar gap occurs between $N_{1v}^{(4)}$ (the minimum of the upper valence band) and $\Gamma_{4v}^{(2)}$ (the maximum of the $B^{III}-X^{VI}$ band). The first heteropolar gap is the smallest for CuAlS₂ (0.01 eV) and is the largest for CuAlSe₂ (0.8 eV). The $B^{III}-X^{VI}$ band represents the weak bond between the $B-X$ atoms. Figure 8 displays the electronic charge density for this band. We have shaded the

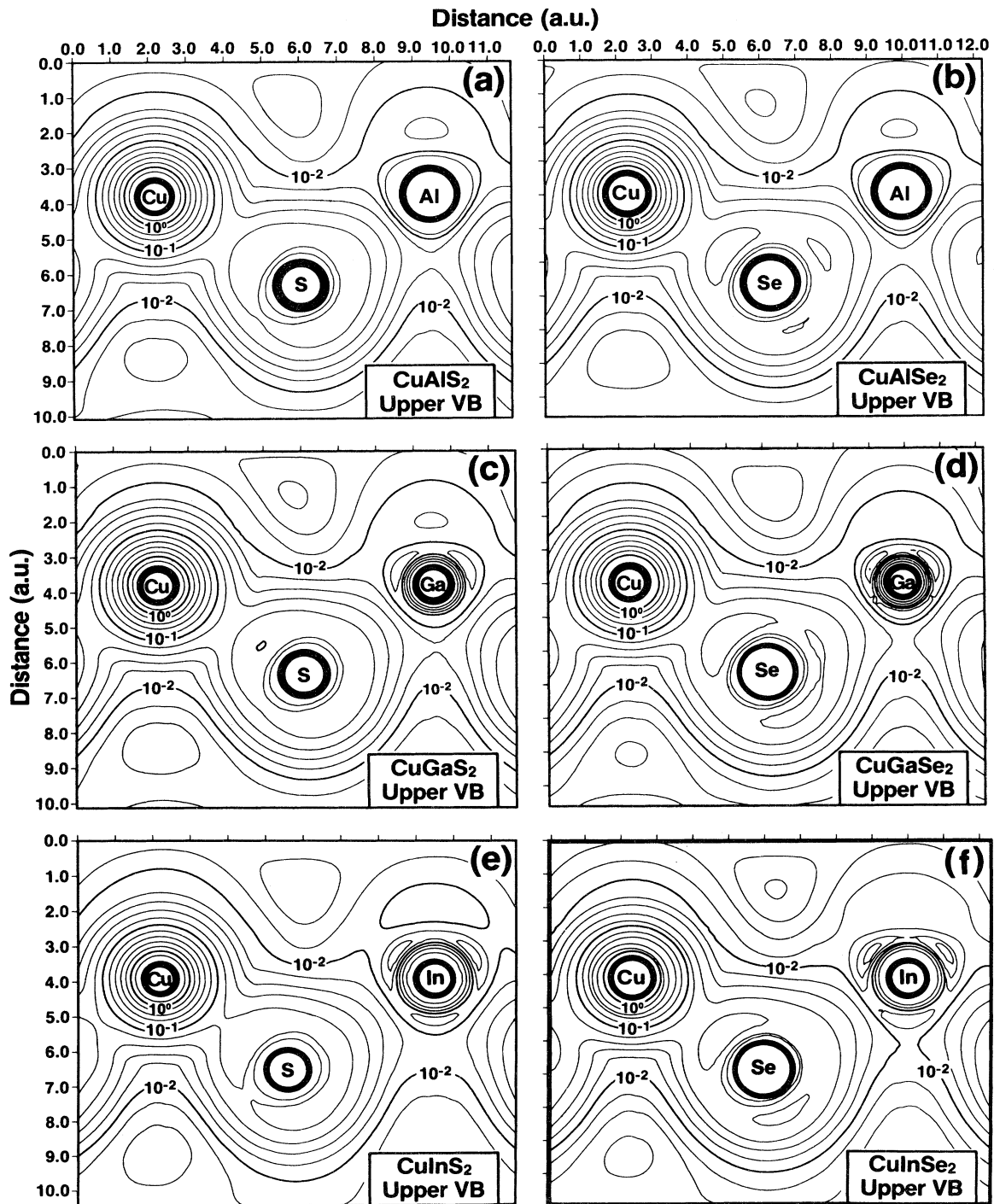


FIG. 6. Calculated electronic charge density for states in the upper valence band (cf. Fig. 5). The contours are logarithmically spaced. (a) CuAlS_2 , (b) CuAlSe_2 , (c) CuGaS_2 (d) CuGaSe_2 , (e) CuInS_2 , and (f) CuInSe_2 . The solid circles denote the core regions, where the rapidly varying charge density was omitted for clarity of display.

logarithmic contours enclosing the charge of $10^{-2} e/a.u.^3$ around the B and X atoms to highlight the regions that contribute to the $B-X$ bond. This charge distribution suggests that the $\text{In}-X$ bond is considerably weaker than

the $\text{Al}-X$ and $\text{Ga}-X$ bonds. The $B^{\text{III}}-X^{\text{VI}}$ band is analogous to the bottom of the upper valence band in binary II-VI semiconductors except that in the ternary analog (column-III rather than column-II cation) it is less ionic-

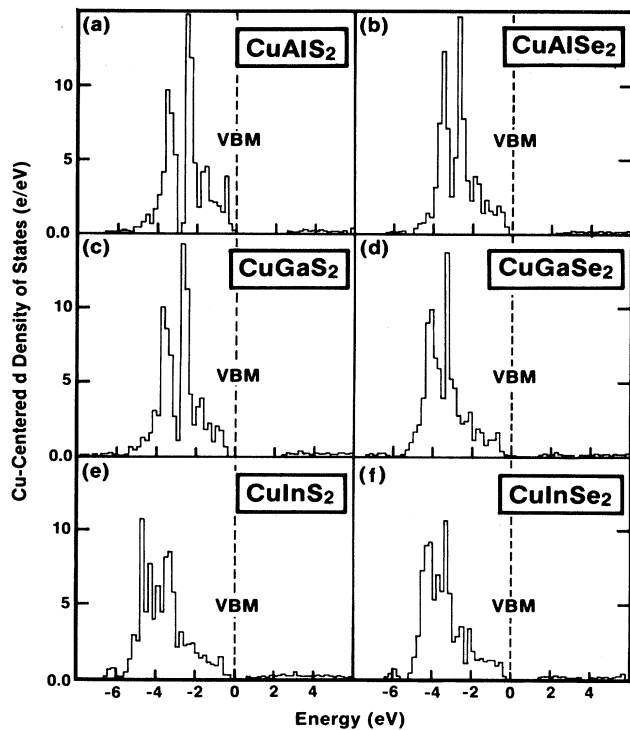


FIG. 7. Cu-centered d -like local density of states of the six group-I chalcopyrites, calculated with Ceperley's correlation. The vertical dashed lines denote the valence-band maximum (VBM).

ly polarized. Such near-tetrahedrally coordinated bonds between a group-III cation and a group-VI anion are unique to these compounds (the GaSe-like polytypes⁴⁰ are not tetrahedral). The width of the $B^{\text{III}}\text{-}X^{\text{VI}}$ band is given by $W_2 = \epsilon(\Gamma_{1v}^{(2)}) - \epsilon(\Gamma_{2v})$ and is the narrowest for the In compounds (~ 0.7 eV) having the weakest $B\text{-}X$ bond. Indeed, the energy separation between the In atomic valence orbitals and the chalcogen atomic p orbitals is considerably larger than the corresponding separation for Al- X and Ga- X pairs,³⁵ leading to narrow $B^{\text{III}}\text{-}X^{\text{VI}}$ bands and to weak bonds for $B = \text{In}$. Partially, this results from the fact that the In- X bands have some Cu d character admixed into them, in contrast to the Al- X and Ga- X bands. The weaker $B\text{-}X$ bonding relative to the $A\text{-}X$ bonding is consistent with the relative ease of forming substitutions on the B^{III} site (rather than on the A site) of ABX_2 compounds (e.g., Fe- B^{III} replacements^{41(a)}} or In-Ga replacements,^{41(b)} particularly for the $A\text{In}X_2$ compounds^{41(c)}). Again, the sulfides have a wider W_2 than the selenides and the order of W_2 , much like the order of W_1 , does not follow the order of the positions of the cations in the Periodic Table but rather the order of atomic orbital energies $W_2^{\text{Ga}} > W_2^{\text{Al}} > W_2^{\text{In}}$ (the s ionization energies for Ga, Al, and In as calculated in the Hartree-Fock model^{35(a)} are 11.55, 10.70, and 10.1 eV, respectively; the observed values^{35(b)} are 11.0, 10.6, and 10.0 eV, respectively). Similarly, the centers of gravity of the $B^{\text{III}}\text{-}X^{\text{VI}}$ bands follow the same atomic order (nonmonotonic with

the position in the column), suggesting that the chemical trends in the binding energies of the $B\text{-}X$ band are controlled by the atomic energies and to a lesser extent by the atomic radii ($R_{\text{Al}} \cong R_{\text{Ga}} < R_{\text{In}}$).

C. The X^{VI} s band

The $B^{\text{III}}\text{-}X^{\text{VI}}$ band is separated from the lower X^{VI} s band by the second heteropolar gap (denoted as "gap 2" in Fig. 5), which is in the range of 5–6 eV. This gap is the largest for the In compounds (6.75 and 6.4 eV for CuInS₂ and CuInSe₂, respectively) and the smallest for the Ga compounds (4.85 and 5.3 eV for CuGaS₂ and CuGaSe₂, respectively). Figure 9 displays the electronic charge density of the X^{VI} s band. The 10^{-2} e/a.u.³ logarithmic contours around the X atoms are shaded to highlight the oval chalcogen s charge. The chalcogen s charge is seen to be slightly elongated toward the B^{III} atomic site. For the In compounds this charge is more ionically localized on the chalcogen site and has the lowest distortion. The width of the chalcogen s band is given by $W_s = \epsilon(\Gamma_{1v}^{(1)}) - \epsilon(\Gamma_{5v}^{(1)})$ and is in the range of 1.2–2 eV. Much like the width W_2 of the $B^{\text{III}}\text{-}X^{\text{VI}}$ band, it is seen that the In compounds give rise to the narrowest bands and to the largest heteropolar gaps. From this point of view, the In compounds can be considered as the most ionic in the series. The sulfur band is considerably deeper than the Se band, following the order of the free-chalcogen s ionization energies.³⁵ Comparing the center of gravity of the $B^{\text{III}}\text{-}X^{\text{VI}}$ and the X^{VI} s bands for the three B^{III} cations, we observe that in all cases the Al compounds have the lowest binding energy, suggesting that the Al site carries the most electronic charge of the three cations. From this point of view, the Al compounds can be considered as the most ionic in the series. Extension of the Phillips–van Vechten dielectric electronegativity model to ternary chalcopyrites⁴² suggests that the In compounds are slightly more ionic than the Al and Ga compounds (electronegativities⁴² of 0.64 and 0.61 for CuInS₂ and CuInSe₂, respectively, compared with 0.59 for CuAlS₂ and CuGaS₂ and 0.55 for CuAlSe₂ and CuGaSe₂), in agreement with the trends in the band widths but in contrast with the trends in the positions of the band centers. We see that a detailed study of the electronic structure reveals that organization of these compounds in a monotonic sequence of decreasing electronegativities depends on which aspect of the band structure is chosen as a guide, and that there is not a unique and universal sorting algorithm for producing an ionicity sequence.

The top of the X^{VI} s band occurs at the Brillouin-zone center and is crystal-field split into $\Gamma_{5v}^{(1)}$ (doubly degenerate) and Γ_{3v} (singly degenerate). This crystal-field splitting is considerably smaller (few hundreds of an electron-volt) than the $\Gamma_{5v}^{(2)}\text{-}\Gamma_{4v}^{(2)}$ splitting at the VBM.

D. The B^{III} d band

The X^{VI} s band is separated by the third heteropolar gap (denoted in Fig. 5 as gap 3) from the narrow B^{III} d

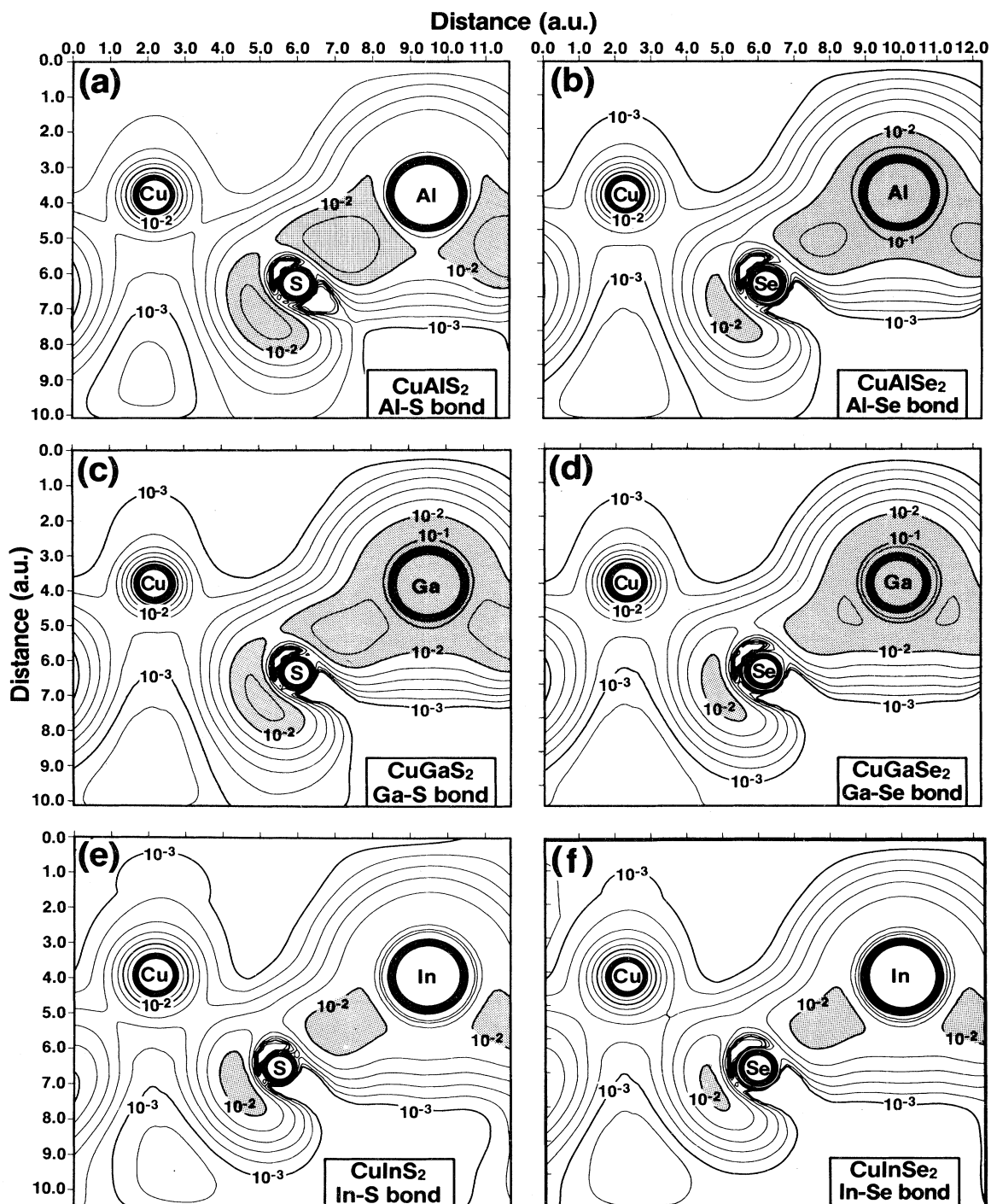


FIG. 8. Calculated electronic charge densities of the $B^{\text{III}}-X^{\text{VI}}$ bands (cf. Fig. 5). The contours are logarithmically spaced. The solid circles indicate the core regions. The $10^{-2} e/a.u.^3$ contours around the B^{III} and X^{VI} atoms are shaded to highlight the $B^{\text{III}}-X^{\text{VI}}$ bond density. (a) CuAlS_2 , (b) CuAlSe_2 , (c) CuGaS_2 , (d) CuGaSe_2 , (e) CuInS_2 , and (f) CuInSe_2 .

band of the Ga and In compounds. The center of gravity of the B^{III} d band follows the order of the atomic nd binding energies,^{35(a)} with Ga $3d$ being somewhat deeper in energy than in the In $4d$. The B^{III} d band behaves as an outer core state and does not participate in bonding.

IV. DENSITY OF STATES

The calculated histogram density of states of the six group-I chalcopyrites is displayed in Figs. 10 and 11. The structure of the various peaks follows the discussion of the various subbands in Sec. III (cf. Fig. 5 for the

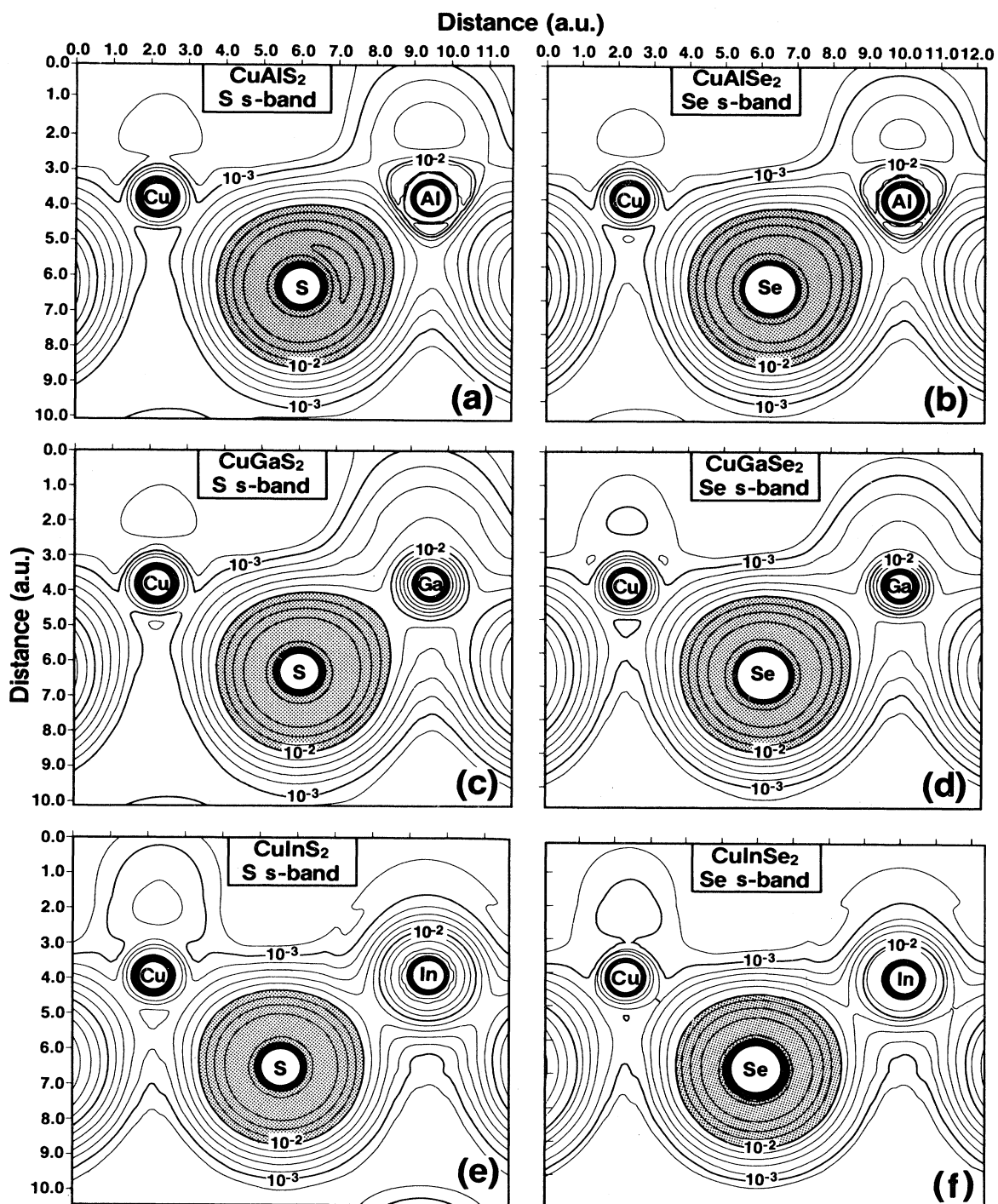


FIG. 9. Calculated electronic charge densities of the X^{VI} s band (cf. Fig. 5). The contours are logarithmically spaced. The solid circles indicate the core regions. The 10^{-2} $e/a.u.^3$ contours around the X^{VI} site are shaded to highlight the X^{VI} s character of these states. (a) CuAlS₂, (b) CuAlSe₂, (c) CuGaS₂, (d) CuGaSe₂, (e) CuInS₂, and (f) CuInSe₂.

schematic subband structure). Where available,^{43–47} the experimental x-ray photoemission (XPS) data are included.

The upper valence band appears as a two-peak struc-

ture, corresponding to the two branches of the Cu d bands (cf. Fig. 7). At higher binding energies we see the $B^{III}-X^{VI}$ bonding band, separated by the second heteropolar gap from the X^{VI} band, the latter separated by the

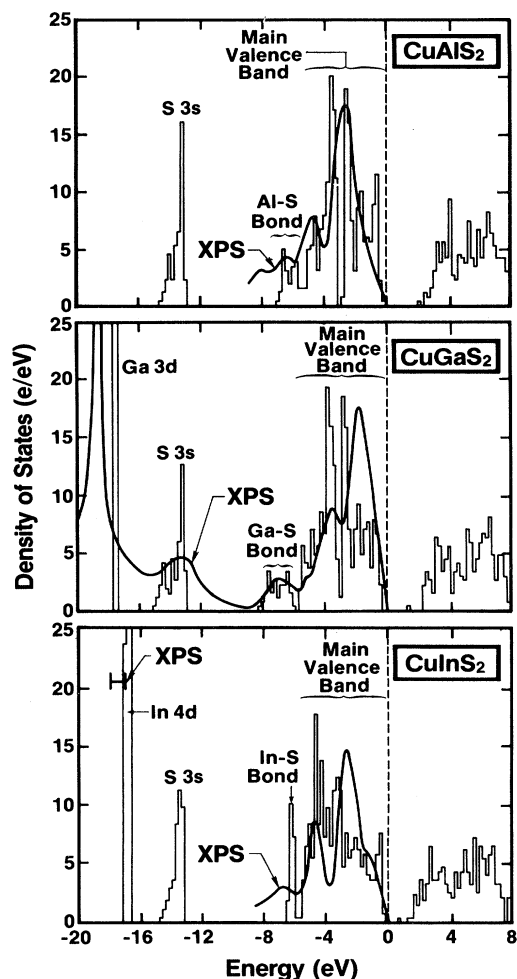


FIG. 10. Calculated density of states histograms for CuAlS_2 , CuGaS_2 , and CuInS_2 . The XPS data are from Refs. 43 and 45 (CuAlS_2), Refs. 44, 45 and 47 (CuGaS_2), and Refs. 45 and 46 (CuInS_2).

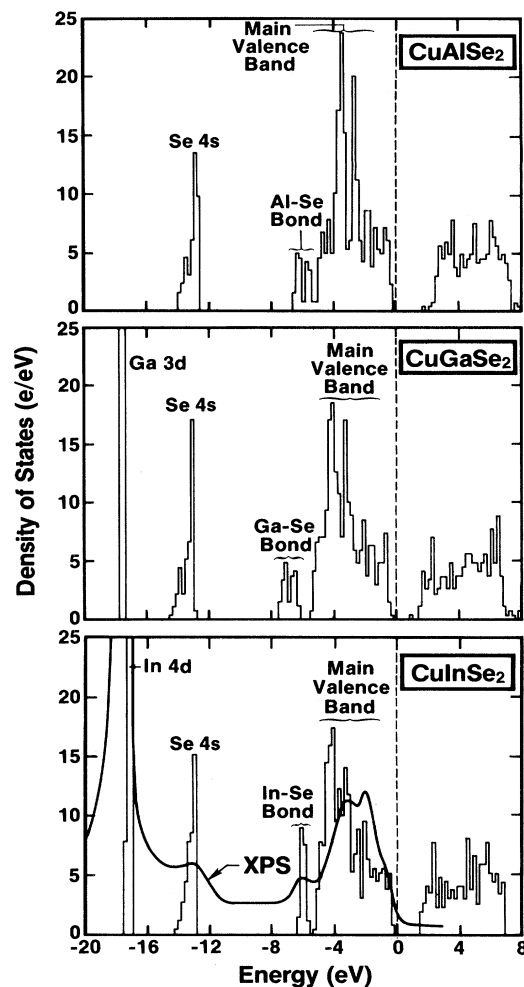


FIG. 11. Calculated density of state histograms for CuAlSe_2 , CuGaSe_2 , and CuInSe_2 . The XPS data for CuInSe_2 are from Ref. 44.

TABLE IV. Comparison of the observed (Refs. 43–47) and calculated positions of the structures in the density of state of group-I chalcopyrites. Results given in eV relative to the $\Gamma_{4v}^{(2)}$ valence-band maximum. The photon energy ($h\nu$) used in the experiment is indicated in the references. The range given in the theoretical results reflects the halfwidth.

States	CuAlS_2		CuGaS_2		CuInS_2		CuAlSe_2	CuGaSe_2	CuInSe_2		
	calc.	expt.	calc.	expt.	calc.	expt.	calc.	calc.	calc.	expt.	
Upper VB											
Cu 3d(1)	2.4	2.7 ^a	2.7	2.9 ^a	3.3	2.3, ^c 2.5 ^a	2.8	3.2	3.3		
Cu 3d(2)	3.4	3.0 ^b	3.7	3.4, ^c 3.4 ^d	4.3	4.3 ^a	3.7	4.1	4.2	3.3 ^c	
$B^{\text{III}}-X^{\text{VI}}$ band	6.1	6.5, ^a 8.4 ^b	6.9	6.7, ^a 7.1 ^c	6.5	6.8 ^c	5.8	6.6	6.0	6.3 ^c	
X^{VI} s band	13.1±0.3	12.0±1.0 ^a	13.1±0.4	13.0, ^c 13.4 ^d	13.2±0.3	12.0±1.0 ^d	12.8±0.3	13.2±0.3	13.0±0.2	13.0 ^a	
B^{III} d band			17.2	18.8–19.3 ^c	16.8	17.4–18.2 ^c		17.5	16.9	17.2–18.0 ^c	
				19.85 ^d							

^aReference 45, $h\nu=1253.6$ eV.

^bReference 43, $h\nu=1253.6$ eV.

^cReference 44, $h\nu=1486.6$ eV.

^dReference 47, $h\nu=1253.6$ eV.

^eReference 46, $h\nu=21.2$ eV.

TABLE V. Calculated (using Ceperley's correlation) [Refs. 27(c) and 29] and measured (room temperature) lowest direct band gaps E_g (in eV) of the six group-I chalcopyrites.

	CuAlS ₂	CuGaS ₂	CuInS ₂	CuAlSe ₂	CuGaSe ₂	CuInSe ₂
E_g^{calc}	2.05	1.25	-0.14	1.65	0.48	~ -0.2
E_g^{expt}	3.49	2.43	1.53	2.71	1.68	0.98

third heteropolar gap from the B^{III} d band in the Ga and In compounds. The present calculation thus allows an unambiguous assignment of all XPS structure. Table IV compares the calculated peaks to the available experimental data and gives predictions for the compounds CuAlSe₂, CuGaSe₂, for which no data could be found in the literature. Given the substantial width of the observed structures, the agreement with experiment is reasonably good, except for the tightly bound B^{III} d bands that are calculated to be at ~ 1 eV too small binding energy. As discussed previously,^{27(a),27(c)} corrections to the local-density theory are predicted to increase the binding energies of tightly bound states and hence go in the right direction. The difference between the calculated and the observed peaks in the upper valence bands is at least partially related to the difficulty of distinguishing experimentally the (photon-energy-dependent) positions of d bands from the anion p components. (The results of Ref. 44 for the X^{VI} s band seem to underestimate consistently the results of Refs. 44 and 47, presumably due to a ~ 1 -eV difference in the assignment of the energy origin in Ref. 45.)

V. CONDUCTION BANDS

Table V compares the calculated and observed³ lowest $\Gamma_{4v}^{(2)} \rightarrow \Gamma_{1c}$ optical band gaps for the six group-I chalcopyrites. As noted in the Introduction and discussed in Ref. 27, the local-density theory²⁶ consistently underestimates the band gaps relative to experiment (e.g., even for the best-studied semiconductors—Si—a nonempirical calculation^{25,27(b)} underestimates the gap by 50%). The errors in the band gaps scale with the percentage of Cu d character, suggesting that they may also scale with the degree of localization of the states. The order of the gaps is correctly reproduced by the theory, in all cases. Since local-density theory usually provides the correct relative

ordering of conduction-band states, we display in Table VI the calculated values relative to the Γ_{1c} state. It is seen that all gaps decrease monotonically with increasing molecular weight in the Al \rightarrow Ga \rightarrow In series, that the gaps of the sulfides are larger than the gaps of the selenides, and that the ΓN^* gaps are smaller than the ΓT^* gaps for all compounds, except the aluminides.

The ternary chalcopyrites are some of the strongest known semiconductor optical absorbers in the solar spectrum. For instance, the linear absorption coefficient of CuInSe₂ at a photon energy $h\nu = 1.5$ eV is⁴⁸⁻⁵⁰ $\sim 10^5$ cm⁻¹, compared with $\sim 7 \times 10^2$ cm⁻¹ for silicon,^{51,52} and 10^3 – 10^4 cm⁻¹ for GaAs (Ref. 53) in the photon energy range of 1.5–1.7 eV. It is easy to see why the absorption at threshold is weaker in homopolar materials (phonon-assisted transitions for indirect-gap semiconductors), but it is less obvious why group-I chalcopyrites absorb stronger than the direct-gap heteropolar binary semiconductors (e.g., GaAs). Our calculation can shed some light on this question.

In direct-gap binary semiconductors, the lowest optical excitation connects a predominantly anionlike state (the VBM at Γ_{15v}) with a predominantly cationlike state (the CBM of GaAs at Γ_{1c} ; away from the Γ_{1c} state there can also be anion character in the CBM if the excited anion s orbitals are energetically close to the cation valence s orbitals).⁵⁴ The excitation across the gap in binary systems hence couples states on the two displaced sublattices and constitutes therefore an "interatomic excitation" which, while dipole allowed, is expected to carry a lower oscillator strength than an intrasite transition. Figures 12 and 13 display the calculated electronic charge densities at the VBM ($\Gamma_{4v}^{(2)}$ state) and CBM (Γ_{1c} state) of CuAlS₂ and CuGaS₂, respectively. It is seen that the transition between the VBM and CBM couples states which have a considerable amplitude on *the same* (anion) sublattice (and to a lesser extent on the Cu site). Owing to the participa-

TABLE VI. Positions of conduction-band states relative to the conduction-band minimum Γ_{1c} (Table V). Values given in eV.

State	CuAlS ₂	CuGaS ₂	CuInS ₂	CuAlSe ₂	CuGaSe ₂	CuInSe ₂
Γ_{1c}	0.0	0.0	0.0	0.0	0.0	0.0
Γ_{3c}	0.47	1.25	2.1	0.64	1.55	2.07
Γ_{2c}	2.05	2.45	2.88	1.85	2.05	2.66
$T_{1c} + T_{2c}$	0.70	1.43	2.17	0.80	1.63	1.84
T_{5c}	1.64	2.0	2.48	1.60	1.60	2.15
$N_{1c}^{(1)}$	1.32	1.28	1.70	0.91	1.00	1.59
$N_{1c}^{(2)}$	2.73	3.14	3.81	2.53	3.17	3.57

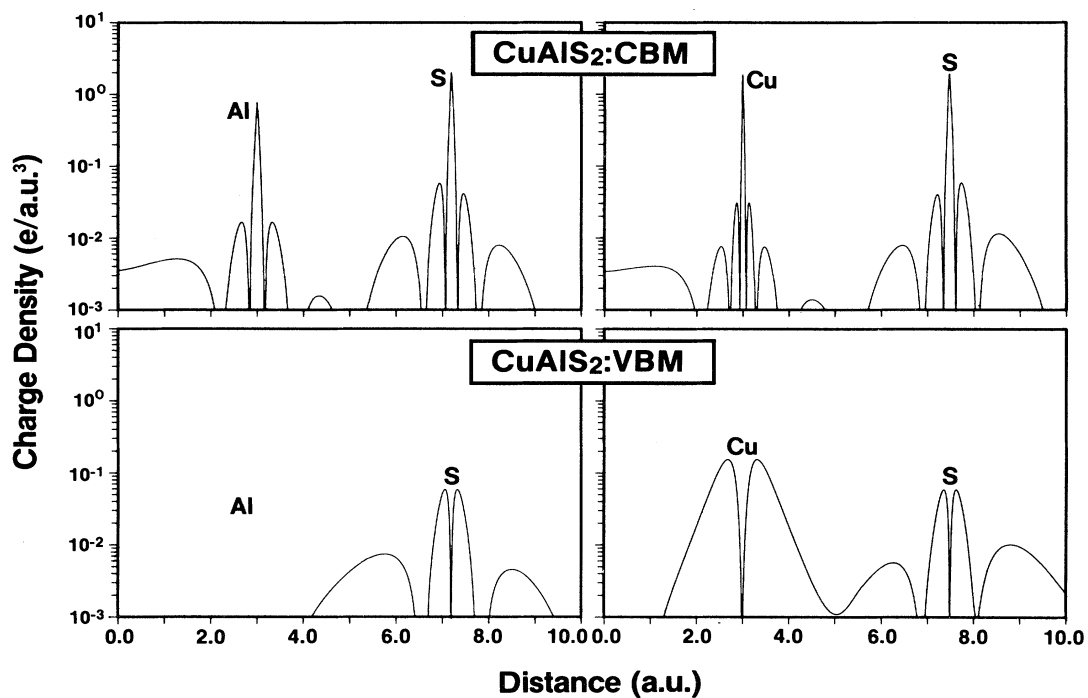


FIG. 12. Electronic charge density at the valence-band maximum (VBM) and conduction-band minimum (CBM) of CuAlS_2 . Note the significant overlap of the sulfur bond charge (and, to a lesser extent, the charge on the Cu site) between the two states.

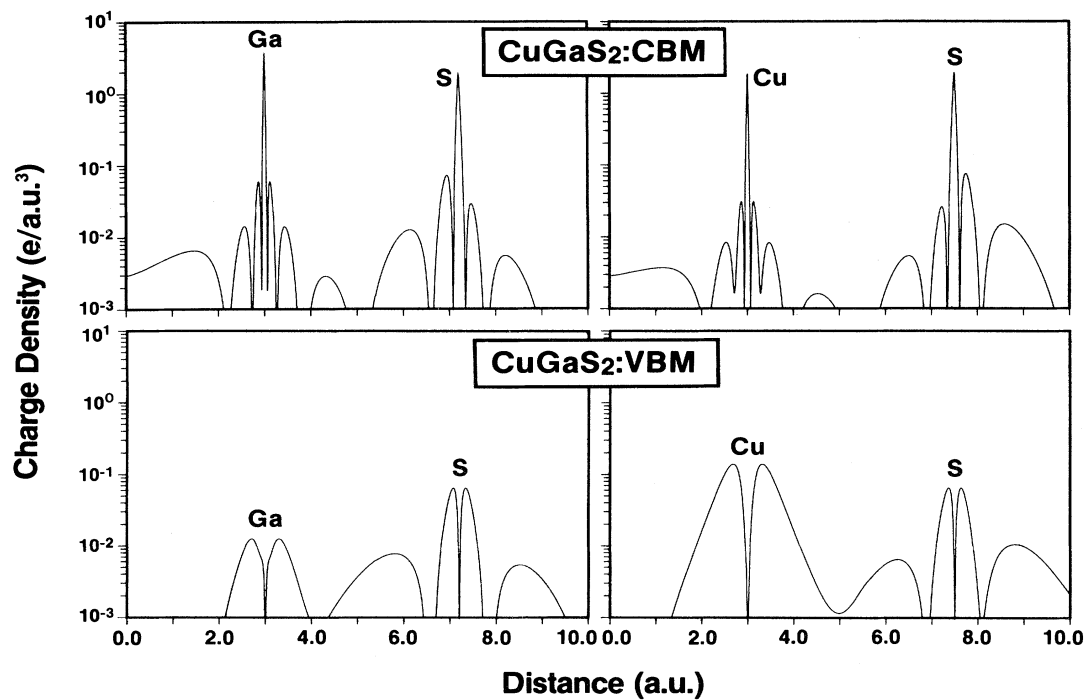


FIG. 13. Electronic charge density at the valence-band maximum (VBM) and conduction-band minimum (CBM) of CuGaS_2 . Note the significant overlap of the sulfur bond charge (and, to a lesser extent, the charge on the Cu site) between the two states.

tion of the Cu *d* orbitals in bonding in the upper valence band, not all of the anion *p* orbitals are consumed in bonding in the valence bands and a significant amount of anion character exists also at the CBM. The VBM → CBM transition in CuBX₂ chalcopyrites hence has an “intra-atomic” component and could be stronger than the analogous interatomic transition in binary semiconductors due to stronger overlap of the initial with the final-state wave functions. This also suggests that the effect of lattice thermal expansion on the temperature dependence of the optical gap will be smaller in chalcopyrites (stronger one-center component to the transitions) relative to binary materials (strong two-center component to the transitions). This is consistent with the anomalously low temperature dependence of the band gap in ternary chalcopyrites,⁵⁵ despite its normal thermal-expansion coefficient.⁵⁶ Likewise, the existence of a significant one-center component to the lowest optical transition in CuBX₂ chalcopyrites is consistent with the anomalously small band-gap pressure coefficient relative to the analogous binary semiconductors.⁵⁷

The calculated structure of levels near the VBM and CBM can be compared with the near-threshold absorption, reflectivity, and electroreflectance data, which show structure at energies above that of the lowest optical transitions (E_g). Such structure has been reported in CuAlS₂, CuGaS₂, CuGaSe₂, and CuInSe₂; it begins roughly 1–1.5 eV above E_g and continues to about 3.0 eV above E_g , with a relatively featureless region separating these structures from a higher-lying spectrum of very strong absorption and reflection features. Four different interpretations have been put forward for the spectrum between $E_g + 1$ eV and $E_g + 3$ eV. (i) In analogy with the zinc-blende compounds, these features in CuAlS₂,⁴⁴ CuGaS₂,^{44,58,59} and CuInSe₂ (Ref. 44) have been identified with E_1 transitions, that is, vertical transitions away from Γ in the Brillouin zone between states at the top of the valence band and others (for the same \vec{k} points) at the bottom of the conduction band. (ii) For CuAlS₂,⁴⁴ CuGaS₂,^{44,59} CuInSe₂,^{44,60,61} and CuGaSe₂,^{62,63} transitions to the conduction-band minimum (Γ_{1c}) from states composed mostly or entirely of Cu *3d* orbitals lying ~ 2 eV below the valence-band maximum have been suggested. (iii) Transitions similar to (ii) but originating in sulfur 3*p* “heavy-hole” bands about 2 eV below the VBM were suggested⁵⁸ to explain structures in this energy region in CuGaS₂. (iv) Gan *et al.*⁶⁴ suggested that pseudodirect transitions from the valence-band maximum Γ_{4v} to the conduction state Γ_{2v} were responsible for strong spectral features in CuInSe₂ in the range 2.5–4.0 eV (1.5–3.0 eV above E_g). Pseudodirect features would normally be very weak, but these authors speculated that their strength and position would be influenced by the partial Cu *3d* character of the states Γ_{4v} and Γ_{5v} at the VBM.

Our results can be used to shed some light on these suggestions. For example, the lowest transitions at the mid-points of the ΓN and ΓT lines of our calculated band structures are all 1.5–2.2 eV above the gaps of the corresponding compounds, implying that the E_1 -type transitions are, indeed, a component of the spectral features in

the range $E_g + 1$ eV → $E_g + 3$ eV for all compounds in this group. Also, there is a cluster of bands at $E_{\text{VBM}} - 2.2$ to $E_{\text{VBM}} - 2.9$ eV which we have found to have very large Cu *3d* character (80–90%). These bands appear as an almost dispersionless group, separated by small gaps from the band above and below them in the Al and Ga compounds. We predict that transitions from these levels will be 2.2–2.9 eV above E_g in reflection and absorption measurements; thus the features in question probably also contain transitions of type (ii). Similarly, just above these highly *d*-like bands we find a pair of bands (one doubly and one singly degenerate at Γ), which can be identified as heavy-hole *p* bands, with a substantial *d*-based admixture. These bands lie 1.6–2.4 eV below their respective valence-band maxima, so they also can contribute to the spectral structures in question [suggestion (iii)].

A few remarks can be added about the higher-lying states at Γ . Transitions from the valence-band maximum to the first two states (Γ_{3c}, Γ_{2c}) above the conduction-band minimum (Γ_{1c}) are pseudodirect: They are derived from indirect transitions in the zinc-blende compounds which are “folded in” to Γ in the chalcopyrite Brillouin zone. These transitions are expected to contribute quite weakly to absorption and reflection when $u \simeq \frac{1}{4}$, since their signature resembles that of an indirect transition. In several of the $A^{II}B^{IV}X_2^V$ compounds the $\Gamma_{4v} \rightarrow \Gamma_{3c}$ transition is the lowest one,⁶⁵ but in all of the $A^{IB}X_2^{VI}$ compounds, the lowest transition is (experimentally⁶⁶) always $\Gamma_{4v} \rightarrow \Gamma_{1c}$, and, in agreement with this, we always find the ordering $\Gamma_{2c} > \Gamma_{3c} > \Gamma_{1c}$. In the Al compounds Γ_{3c} is closer to Γ_{1c} than to Γ_{2c} , while in CuGaS₂ Γ_{3c} is midway between the other two, and in the In compounds Γ_{3c} is closer to Γ_{2c} ; numerical values are given in Table VI. Our values for $\epsilon_{\Gamma_{2c}} - \epsilon_{\Gamma_{1c}}$ are consistent with the proposal of Gan *et al.*⁶⁴ that the strong reflectance features 1.5–3 eV above E_g are partly due to $\Gamma_{4v,5v} \rightarrow \Gamma_{2c}$ transitions; for the In and Ga compounds, Γ_{3c} might contribute also. However, our results also indicate that E_1 -type transitions away from Γ and transitions to Γ_{1c} from the closely-spaced states below the top of the valence band are present in this same energy range for all six compounds. Thus we predict that the pseudodirect transitions make (at most) a rather small contribution to the observed spectral properties of the $A^{IB}X_2^{VI}$ chalcopyrites.

VI. COMPARISON WITH OTHER CALCULATIONS

Table VII compares the present results for the band structure of CuAlS₂ and CuGaSe₂ with the results of the empirical local-pseudopotential calculation of Poplavnoi^{20,21} and the numerical LCAO results of Oguchi *et al.*²³ at the Brillouin-zone center. It is seen that the numerical LCAO calculation produces fundamental band gaps that are considerably smaller than those predicted by the present calculation, presumably due to the small basis set used in Ref. 23. Indeed, convergence tests (cf. Sec. II and Ref. 25) indicate that one obtains anomalously small band gaps if small basis sets are used. The empirical local pseudopotential calculation of Ref. 21 produces in most

TABLE VII. Comparison of the present band structure with that of Poplavnoi *et al.* (Ref. 21) and Oguchi *et al.* (Ref. 23) at the Brillouin-zone center. The VBM is set as the zero of energy.

State	CuAlS ₂			CuGaS ₂		
	Present	Ref. 23	Ref. 21	Present	Ref. 23	Ref. 21
Upper VB						
$\Gamma_{4p}^{(2)}$	0.0	0.0	0.0	0.0	0.0	0.0
$\Gamma_{5p}^{(2)}$	-0.32	-0.24	-0.14	-0.32	-0.22	-0.12
$\Gamma_{4p}^{(1)}$	-4.63	-5.73	-3.20	-4.85	-5.48	-3.45
B^{III}-X^{VI} band						
$\Gamma_{1p}^{(2)}$	-4.93	-6.51	-4.26	-5.71	-6.55	-3.75
$\Gamma_{2p}^{(2)}$	-6.74	-7.72	-6.78	-8.00	-8.08	-5.89
X^{VI} s band						
$\Gamma_{5p}^{(1)}$	-12.81	-13.84	-11.52	-12.85	-13.07	-15.04
$\Gamma_{3p}^{(1)}$	-12.83	-13.72	-11.72	-12.89	-12.98	-15.28
$\Gamma_{1p}^{(1)}$	-14.32	-15.22	-13.38	-14.87	-14.92	-16.08
B^{III} d band						
				-17.2±0.38	-15.64 to -15.96	
Conduction band						
Γ_{1c}	2.05	0.72	3.66	1.25	0.54	2.95
Γ_{3c}	2.52	2.27	3.31	2.50	2.66	4.91
Γ_{2c}	4.10	4.70	4.72	3.70	4.04	5.71
Γ_{5c}	5.27	4.83	5.87	5.06	5.23	6.84
Γ_{4c}	5.95	5.71	5.90	5.55	5.80	7.58
Γ_{5c}	5.65	5.75	6.55	5.51	5.48	7.96

cases the correct ordering of bands, and the gaps are qualitatively right. However, since this model neglects the Cu *d* orbital effects, it tends to produce larger gaps and narrower bands than the present results. This is consistent with the discussions of Sec. III A and Ref. 36, which indicate that the omission of active Cu 3*d* states tends to dramatically increase the band gaps. The results of Ref. 23 predicted that the Ga 3*d* band in CuGaS₂ is ~1.5 eV higher in energy than in the present study. Since even a small basis set should be adequate to describe this nearly atomic band, the difference suggests that in the results of Ref. 23 the B atom carries more electronic charge (i.e., lower binding energy) than in the present calculation. Indeed, we find a similar result in our own study when self-consistency is not carried out to completion, yielding an ionically polarized B^{III}-X^{VI} bond with a spuriously low B^{III} binding energy.

VII. X-RAY SCATTERING FACTORS

We have calculated the Fourier transform of the electronic charge density (x-ray structure factors) for six group-I chalcopyrites. The reciprocal-lattice vectors \vec{G} of the chalcopyrite structure can be divided into three groups.⁶⁷ Denoting the components of \vec{G} by the three integers $\vec{G} = (2\pi/a)(n, m, l/2\eta)$, these groups are as follows: (i) (n, m, l) all even or all odd; (ii) (n, m) even, l odd; (iii) n

even, m, l odd, or (n, l) odd, m even. The significance of this partitioning is that if the electronic charge density $\rho(\vec{r})$ [or crystal potential $V(\vec{r})$] is written as a superposition of atomic charge densities $f_\alpha(\vec{r})$ [or atomic potentials $v_\alpha(\vec{r})$] of types $\alpha = A, B, X$, then the Fourier transform $\rho(\vec{G})$ [or $V(\vec{G})$] falls into three groups according to the types (i)–(iii) of the vector \vec{G} . Specifically,

$$\rho_1(\vec{G}) = [f_A(\vec{G}) + f_B(\vec{G}) + f_X(\vec{G})]g_1(n, m, l; u), \quad (1)$$

$$\rho_2(\vec{G}) = \pm f_X(\vec{G})g_2(n, m, l; u), \quad (2)$$

$$\rho_3(\vec{G}) = \frac{1}{2}[f_A(\vec{G}) - f_B(\vec{G})]g_3^{(1)}(n, m, l, u) + 2f_X(\vec{G})g_3^{(2)}(n, m, l; u), \quad (3)$$

where g_1, g_2, g_3 denote trigonometric functions.⁶⁷ The scattering factors of group (i) [Eq. (1)] evolve from the zinc-blende (ZB) reciprocal-lattice vectors $\vec{G}_{ZB}(\Gamma)$ corresponding to the sum of the atomic factors $f_\alpha(\vec{G})$ of all three types of atoms in the unit cell. The scattering factors of group (ii) [Eq. (2)] evolve from the ZB reciprocal-lattice vectors $\vec{G}_{ZB}(X)$ and involve the anion alone. The scattering factors of group (iii) [Eq. (3)] correspond to the ZB reciprocal-lattice vectors $\vec{G}_{ZB}(W)$ and involve the difference between the cation structure factors [first term in Eq. (3)] as well as the anion contribution [second term in Eq. (3)]. For an undistorted anion sublattice ($u \equiv \frac{1}{4}$), the geometrical factors $g_2 \equiv g_3^{(2)} = 0$ and hence $\rho_2(\vec{G}) \equiv 0$

TABLE VIII. Calculated x-ray scattering factors of the six group-I ternary chalcopyrites, in units of e/cell . The reciprocal-lattice vectors are divided into three groups [(i)-(iii)]. Group (i) denotes the zinc-blende-like factors, group (ii) denotes the anion factors (vanishes for $u = \frac{1}{4}$), and group (iii) denotes the cation ionicity factors, cf. Eqs. (1)–(3). The maximum error bars are estimated at $\pm 0.3e/\text{cell}$.

Reciprocal-lattice vectors	$u = 0.275$ CuAlS ₂	$u = 0.275$ CuGaS ₂	$u = 0.214$ CuInS ₂	$u = 0.269$ CuAlSe ₂	$u = 0.250$ CuGaSe ₂	$u = 0.224$ CuInSe ₂
Group (i)						
0,0,0	148.00	184.00	220.00	220.00	256.00	292.00
1,1,1	84.28	112.77	142.63	134.67	155.16	177.98
2,0,0	21.38	53.32	84.94	42.77	12.09	21.26
0,0,2	20.21	51.98	82.78	44.09	11.97	18.34
2,0,2	94.56	123.04	151.57	155.88	186.54	214.09
2,2,0	94.10	122.86	149.43	155.21	187.21	211.47
1,1,3	62.94	86.21	112.28	106.02	122.84	142.81
3,1,1	62.56	86.43	111.01	104.59	123.56	139.70
2,2,2	19.90	45.67	73.50	34.50	10.71	19.66
4,0,0	76.69	100.70	122.42	129.69	159.10	176.28
0,0,4	78.73	102.12	129.07	132.76	157.55	185.18
3,3,1	53.02	73.29	94.81	89.70	107.69	119.29
1,3,3	53.49	73.30	95.81	91.13	107.19	121.99
2,0,4	14.46	36.19	61.00	33.20	11.85	12.92
2,4,0	17.69	39.84	66.66	28.89	11.79	21.36
4,0,2	16.87	38.91	65.17	29.99	11.80	19.19
4,2,2	66.78	87.49		113.69	140.56	
Group (ii)						
2,0,1	1.11	1.09	2.14	1.56	0.00	2.82
3,1,2	1.56	1.56	3.28	2.43	0.00	4.65
1,3,0	1.75	1.75	3.55	2.67	0.00	4.98
2,0,3	0.76	0.76	1.72	1.21	0.00	2.40
4,0,1	2.98	2.98	6.11	4.66	0.00	8.78
4,2,1	2.13	2.13	4.30	3.31	0.00	6.19
Group (iii)						
1,0, $\frac{1}{2}$	17.85	6.63	19.56	14.85	2.23	15.78
3,0, $\frac{3}{2}$	8.35	10.25	9.17	0.56	2.38	1.45
2,1, $\frac{3}{2}$	16.30	8.13	19.31	17.38	2.31	21.30
4,1, $\frac{5}{2}$	16.78	8.63	23.95	24.65	2.57	34.07
4,1, $\frac{3}{2}$	18.00	8.93	24.96	26.26	2.55	35.70
2,1, $\frac{1}{2}$	23.87	6.85	29.11	29.16	2.20	36.08
3,2, $\frac{5}{2}$	20.57	6.44	28.84	29.38	2.65	40.33
3,2, $\frac{1}{2}$	9.30	11.24	11.67	10.47	2.40	14.62
3,0, $\frac{1}{2}$	25.53	5.99	32.57	34.47	2.36	44.11
3,0, $\frac{5}{2}$	7.14	9.75	8.74	0.08	2.42	1.22
1,0, $\frac{3}{2}$	24.73	1.75	29.38	28.01	2.00	33.50
3,2, $\frac{3}{2}$	22.35	6.83	30.30	31.68	2.52	42.48
1,4, $\frac{1}{2}$	14.69	10.42	19.58	21.36	2.49	28.50
1,2, $\frac{5}{2}$	14.40	7.26	18.09	15.45	2.34	19.88
3,0, $\frac{7}{2}$	19.30	4.25	27.45	26.79	2.55	37.18
1,0, $\frac{5}{2}$	21.18	0.71	26.28	24.47	2.35	30.36
1,2, $\frac{7}{2}$	16.80	4.70	23.34	21.42	2.54	29.31
1,0, $\frac{7}{2}$	12.63	4.98	15.86	10.42	2.44	12.61
1,0, $\frac{9}{2}$	10.23	4.75	14.46	8.35	2.50	11.64

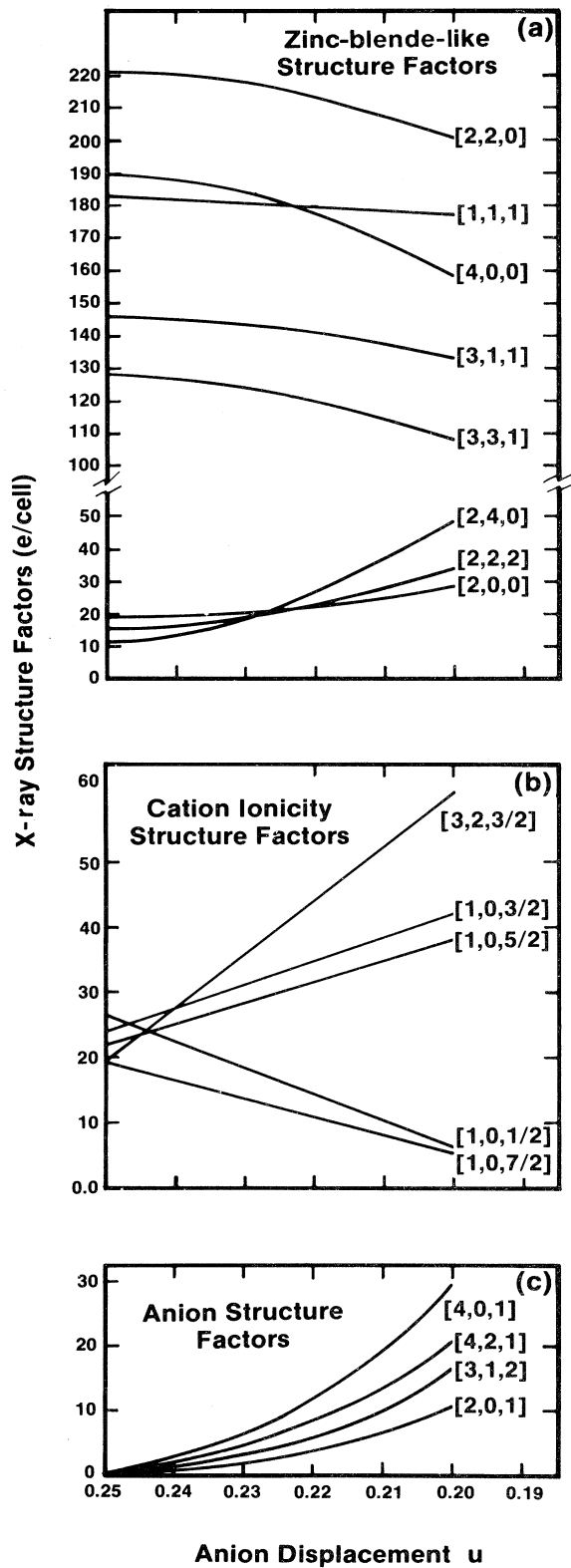


FIG. 14. Variation of the x-ray scattering amplitudes of CuInSe_2 with the anion displacement parameter u . The Slater exchange has been used in this calculation. (a) Group (i) [Eq. (1)]; (b) Group (iii) Eq. (3); (c) Group (ii) [Eq. (2)].

and $\rho_3(\vec{G}) = \rho_3(\vec{G}) = \frac{1}{2}[f_A(\vec{G}) - f_B(\vec{G})]g_3^{(1)}$. We hence refer to $\rho_2(\vec{G})$ as the "anion factor" and to $\rho_3(\vec{G})$ as the "cation ionicity factor."

Table VIII lists the calculated x-ray scattering factors of the six group-I ternary chalcopyrites,⁶⁸ arranged according to the three groups of reciprocal-lattice vectors. In the calculation we have not assumed that the charge density in the crystal can be approximated as a superposition of atomic charge densities [cf. Eqs. (1)–(3)], but have rather taken a direct Fourier transform of $\rho(\vec{r})$. It is seen that for CuGaSe_2 having $u = \frac{1}{4}$, all of the anion factors [group (ii)] are zero. This suggests that the u dependence of the structure factors may contain useful information on the ionicity of the system. We have calculated the band structure of CuInSe_2 self-consistently as a function of the anion displacement parameter u in the range $u = 0.25$ (equal bonds) to $u = 0.20$, going through the experimental equilibrium value of $u = 0.224$. Figure 14 displays the variations in some of the structure factors with u . It shows that as u increases towards 0.25 (i.e., the two cation-anion bond lengths tend to equalize) the strong zinc-blende-like scattering amplitudes [belonging to group (i)] increase, suggesting that the band gap will increase.³⁶ The cation ionicity structure factors [Fig. 14(b), group (iii)] all converge to a narrow region. Their values at $u = \frac{1}{4}$ measure the asymmetric scattering factors [Eq. (3)] and hence the ionicity of the cation sublattices. The calculation clearly shows the larger Cu-In polarity relative to that of the Cu-Ga pair [compare Fig. 14(b) with the CuGaSe_2 results of Table VIII]. Hence such $\rho(\vec{G})$ vs u calculations can provide a direct and unambiguous measure for the cation ionicities in ABX_2 compounds. The strong variations found for group (ii) amplitudes [Figs. 14(c) and 14(b), respectively] further suggest that such calculations could be used to deduce the experimental u value by fitting the observed $\rho(\vec{G})$ to the calculated curves.

To compare the calculated structure factors $\rho(\vec{G})$ with the experimental values⁶⁹ one has to deconvolute from the latter quantities the Debye-Waller temperature factors and the dispersion corrections. Unfortunately, there is no simple and unique way to do this since the crystallographic structure refinement procedures⁶⁹ assume in determining the temperature coefficients that the crystalline density

TABLE IX. Examples of calculated (using an anion displacement parameter $u = 0.275$) and observed (Ref. 69) structure factors of CuGaS_2 .

Beam	Theory uncorrected $\rho(\vec{G})$	Theory corrected $\rho(\vec{G})\bar{T}(\vec{G})$	Expt. (Ref. 69) $\bar{\rho}(\vec{G})$
1,1,1	112.77	109.71	108.90
2,0,0	53.32	52.24	54.55
2,2,0	122.86	114.21	114.50
3,1,1	86.43	80.69	81.70
2,2,2	45.67	40.93	42.05
2,4,0	39.84	31.66	32.80
4,2,2	87.49	73.71	79.15

$\rho(\vec{r})$ can be described as a superposition of spherical atomic charge densities $\rho_{\alpha}^{\text{atom}}(\vec{r}-\vec{r}_{\alpha})$ at sites \vec{r}_{α} . In contrast, the full band-structure calculations make no use of such simple approximations and hence produce a nonzero

bonding charge

$$\Delta(\vec{r}) \equiv \rho(\vec{r}) - \sum_{\alpha} \rho_{\alpha}^{\text{atom}}(\vec{r}-\vec{r}_{\alpha}).$$

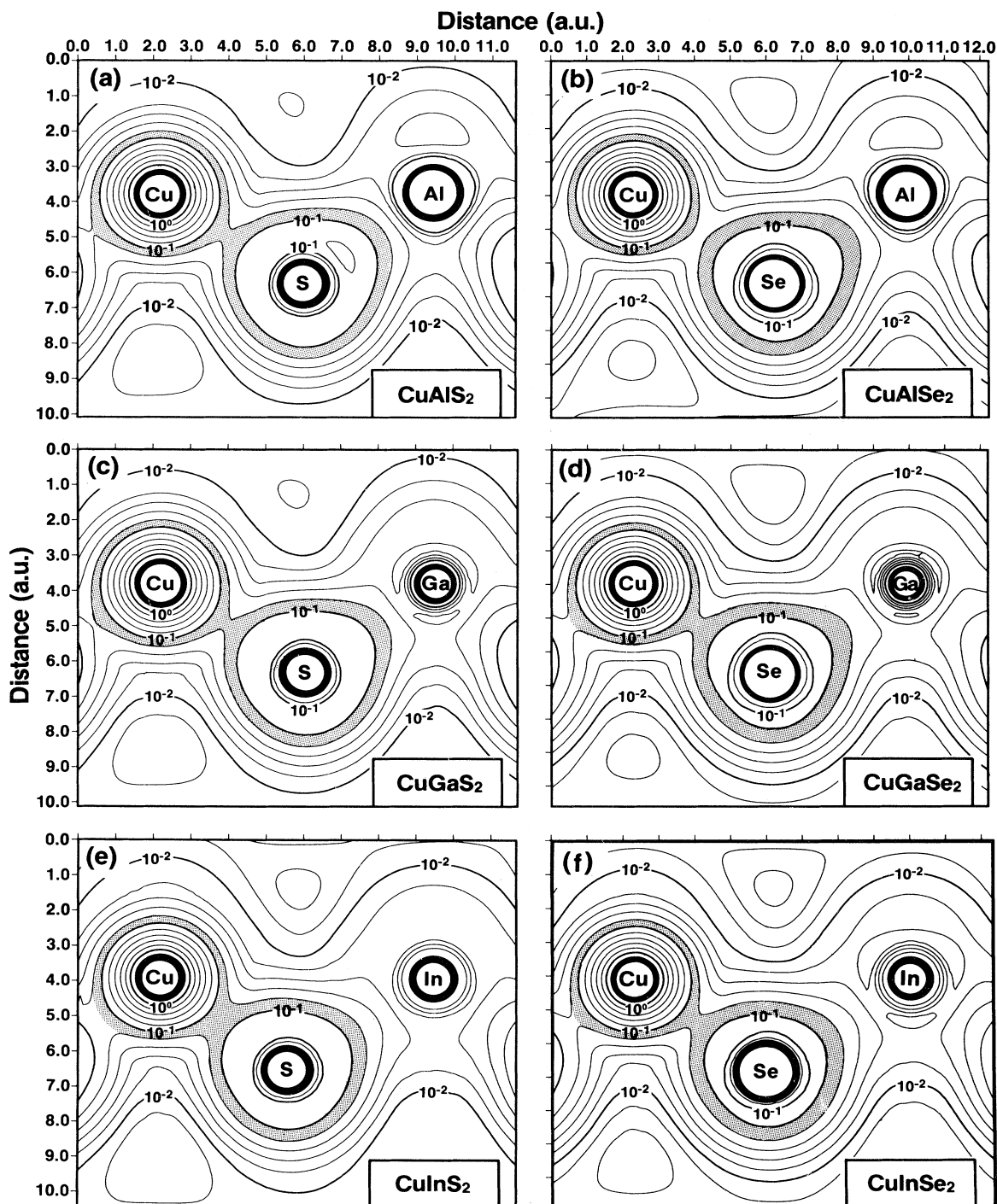


FIG. 15. Contour plots of the total valence electronic charge density of the six group-I ternary chalcopyrites. The contours are logarithmically spaced. The solid circles denote the core regions. The 8×10^{-2} to 10^{-1} e/a.u.³ contours are shaded to highlight the covalent $A^{\text{I}}-X^{\text{VI}}$ bond. (a) CuAlS₂, (b) CuAlSe₂, (c) CuGaS₂, (d) CuGaSe₂, (e) CuInS₂, and (f) CuInSe₂.

Nevertheless, one can devise an approximate procedure to compute the average correction factors. In the crystallographic superposition model⁶⁹ one describes an approximate temperature-corrected structure factor $\tilde{\rho}(\vec{G}_{hkl})$ at the reciprocal-vector \vec{G}_{hkl} (where h , k , and l are the Miller indices) as

$$\tilde{\rho}(\vec{G}_{hkl}) = \sum_{\alpha=1}^M \rho_{\alpha}^{\text{atom}}(\vec{G}_{hkl}) T_{\alpha}^{hkl} e^{-i \vec{G}_{hkl} \cdot \vec{\tau}_{\alpha}}, \quad (4)$$

where $M=8$ is the number of atoms per unit cell, $\vec{\tau}_{\alpha}$ is the position of the α th atomic site in the unit cell, and T_{α}^{hkl} is the α th temperature factor, given as

$$T_{\alpha}^{hkl} = e^{-\vec{G}_{hkl} \cdot \vec{\beta}_{\alpha} \cdot \vec{G}_{hkl}}, \quad (5)$$

where $\vec{\beta}_{\alpha}$ is the anisotropic temperature coefficient tensor. One can hence define a density-weighted average of the temperature factors in the superposition model as

$$\bar{T}^{hkl} = \frac{\sum_{\alpha=1}^M \rho_{\alpha}^{\text{atom}}(\vec{G}_{hkl}) T_{\alpha}^{hkl} e^{-i \vec{G}_{hkl} \cdot \vec{\tau}_{\alpha}}}{\sum_{\alpha=1}^M \rho_{\alpha}^{\text{atom}}(\vec{G}_{hkl}) e^{-i \vec{G}_{hkl} \cdot \vec{\tau}_{\alpha}}}. \quad (6)$$

These factors can be evaluated from the experimental anisotropic temperature coefficients $\vec{\beta}_{\alpha}$ and the spherical atomic structure factors $\rho_{\alpha}^{\text{atom}}(\vec{q})$ used in the empirical structure refinement.⁶⁹ The calculated $\rho(\vec{G}_{hkl}) \bar{T}_1^{hkl}$ can then be compared with the experimental structure factors

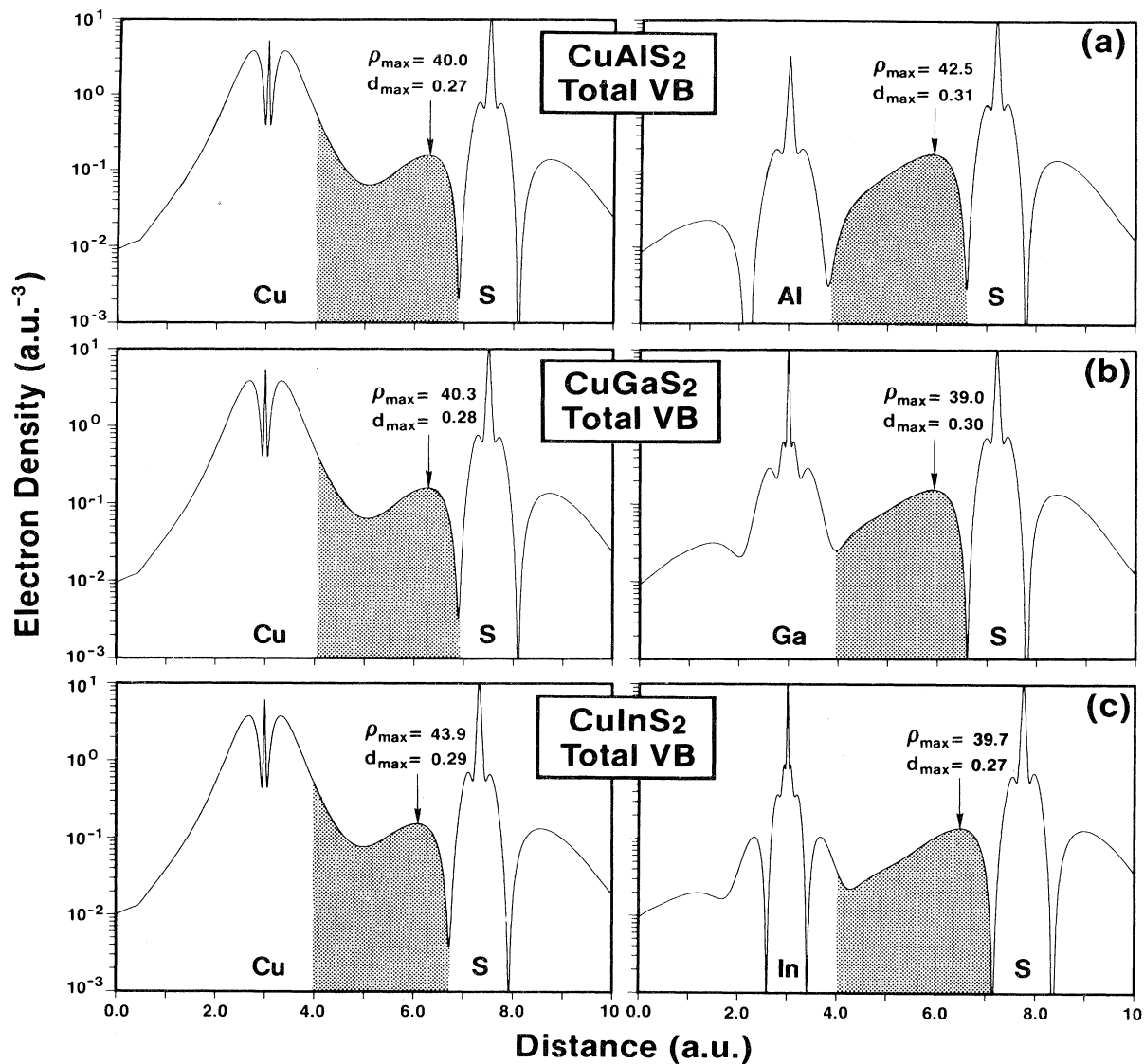


FIG. 16. Line plots of the valence charge densities (in units of $e/\text{a.u.}^3$) along the $A-X$ and $B-X$ bonds in the sulfides. The shaded areas denote the bond charge outside the core radii taken as $\frac{1}{2}(r_s^\alpha + r_p^\alpha)$, where r_s and r_p are the density-functional orbital radii of Ref. 71. d_{max} denotes the distance from the anion, in units of the bond length R_{AX} or R_{BX} , at which the charge density reaches its maximum value ρ_{max} . The latter is given in units of e/cell .

$\bar{\rho}(\vec{G}_{hkl})$. One could also replace Eq. (6) by a simple average of the temperature coefficients over atoms, yielding a different approximation \bar{T}_2 of the form:

$$\log_{10} \bar{T}_2^{hkl} = \frac{1}{M} \sum_{\alpha=1}^M \log_{10} T_{\alpha}^{hkl}. \quad (7)$$

For the ternary chalcopyrites examined we find that \bar{T}_2 is within 5% of the more exact expression \bar{T}_1 . Table IX compares for CuGaS₂ a few of the calculated and measured structure factors belonging to the lowest beams of group (i) reflections. The agreement is improved considerably relative to the temperature-independent structure factors (Table VIII). Notice that one can now define a new procedure for determining the anion displacement param-

eter u by varying u to minimize the difference between the calculated and observed structure factors. This can be done given the u variations of the calculated structure factors (Fig. 14). We indeed find that the agreement between theory and experiment (last two columns of Table IX) can be improved further if instead of using $u = 0.275$ (the experimental value of Ref. 33) we use $u = 0.254$ (the experimental value of Ref. 69). For example, the temperature corrected value for $hkl = 422$ is 73.71 using $u = 0.275$ and 78.24 using $u = 0.254$, compared with the observed value of 79.15. We suggest that this new refinement procedure, based on a self-consistently calculated charge density, is an improvement over the classical procedure used in crystallography,⁶⁹ where one constrains the crystal density to be given as a superposition of spherical objects centered on

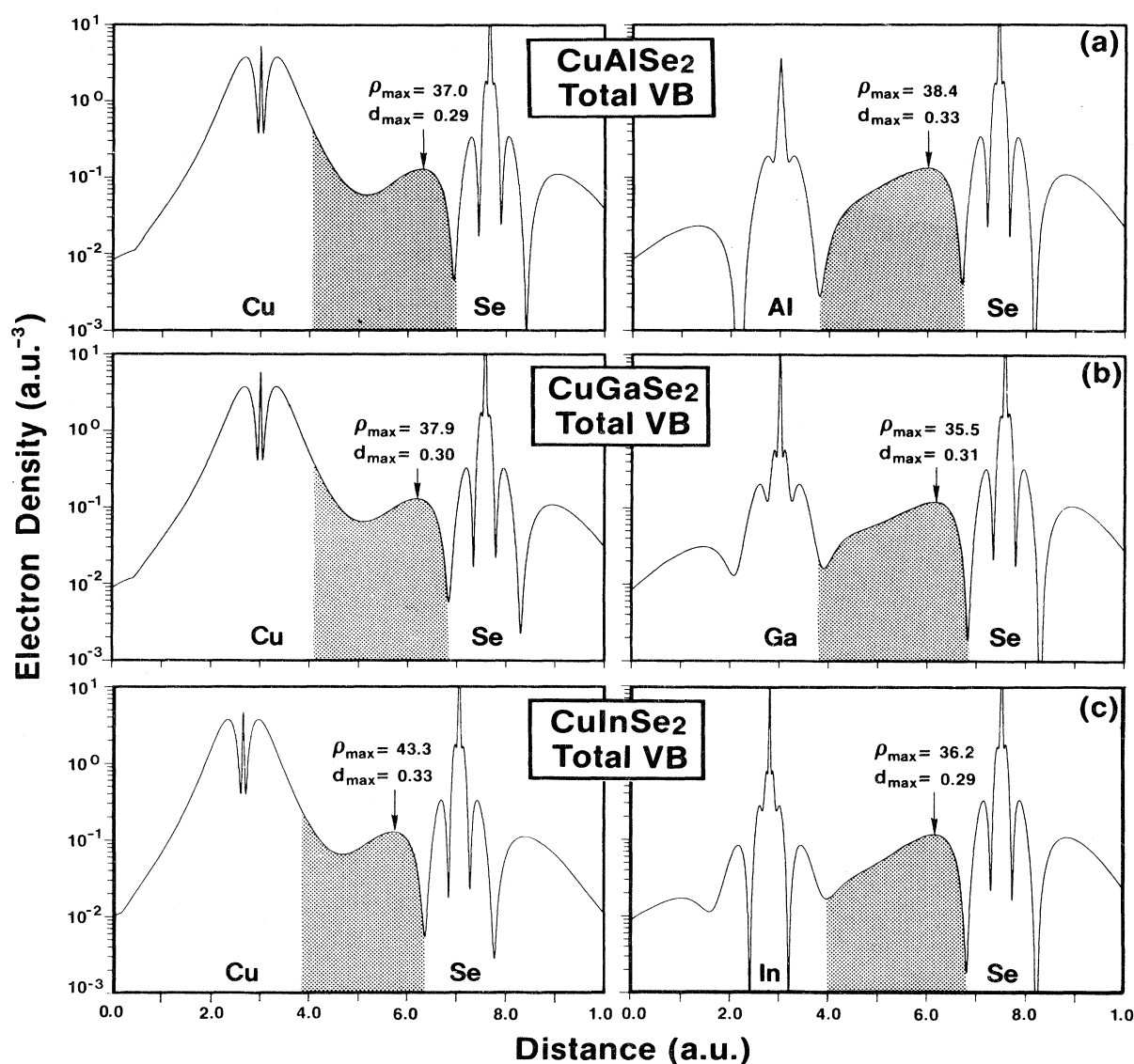


FIG. 17. Line plots of the valence charge densities (in units of $e/a.u.^3$) along the $A-X$ and $B-X$ bonds in the selenides. The shaded areas denote the bond charge outside the core radii taken as $\frac{1}{2}(r_s^\alpha + r_p^\alpha)$, where r_s and r_p are the density-functional orbital radii of Ref. 71. d_{\max} denotes the distance from the anion, in units of the bond length R_{AX} or R_{BX} , at which the charge density reaches its maximum value ρ_{\max} . The latter is given in units of e/cell .

atomic sites and finds $\rho(\vec{G})$ and u within these constraints.

VIII. ELECTRONIC CHARGE DISTRIBUTION

Figure 15 displays the total electronic charge density of the six group-I chalcopyrites. The shading of the $8 \times 10^{-2} - 10 \times 10^{-2} e/a.u.^3$ regions highlights the charge surrounding the A^I-X^{VI} bond. It is seen that whereas the A^I-X^{VI} bond appears like a bonding contact, the $B^{III}-X^{VI}$ bond appears nonbonding. As discussed in Sec. III A, this behavior is dictated primarily by the charge density of the upper valence band (cf. Fig. 6). However, although the A^I-X^{VI} bond is surrounded by a "peanut-shaped" lobe of charge (shaded areas in Fig. 15) as in clas-

sical covalent bonds, the charge density along this bond is clearly polarized towards the anion site, indicating its partial ionic character. This can be better appreciated in line plots of the electron densities (Figs. 16 and 17). In these figures we show the spatial variations of the charge along the $A-X$ and $B-X$ near-neighbor bond directions for the sulfides (Fig. 16) and the selenides (Fig. 17). To delineate the bond charge from the core charge we have inscribed spheres around each site α with a radius $\frac{1}{2}(r_s^\alpha + r_p^\alpha)$, where r_s and r_p are the density-functional orbital radii for s and p orbitals, respectively, calculated previously.⁷⁰ We have shaded the area between the boundaries of these core radii to highlight the bond charge. It is seen that the orbital radii, calculated for *free atoms*⁷⁰ correspond very closely to the position of the outer nodes of the chalcogen wave

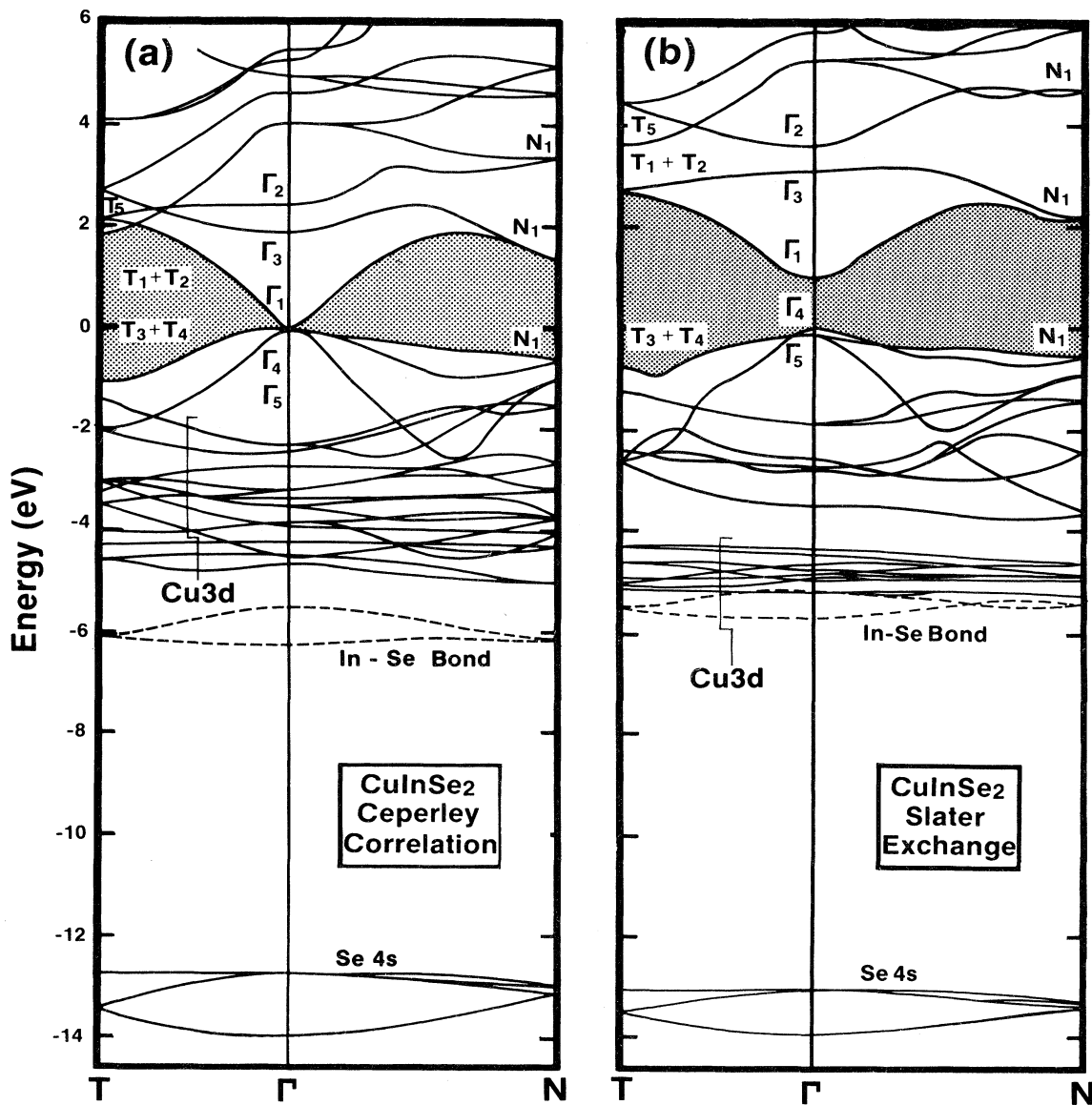


FIG. 18. Comparison of the electronic band structure of CuInSe_2 with (a) the Ceperley correlation; (b) the Slater exchange with $\alpha=1.1$.

functions in the *solid*, highlighting the transferability of these radii. d_{\max} denotes in Figs. 16 and 17 the distance from the anion sites (in units of the corresponding bond distances) at which the charge density reaches its maximum ρ_{\max} .

A number of chemical trends are evident. First, the charge along the $A-X$ bond is generally more polarized towards the anion site than the charge along the $B-X$ bond, i.e., $d_{\max}^{AX} < d_{\max}^{BX}$, suggesting the higher polarity of the $A-X$ charge distribution relative to the $B-X$ distribution. Second, whereas the sequence of increasing polarity (i.e., decreasing d_{\max}) along the A^I-X^{VI} bonds is $\text{In} < \text{Ga} < \text{Al}$, the sequence is reversed along the $B^{III}-X^{VI}$ bonds, i.e., $\text{Al} < \text{Ga} < \text{In}$. The peak values of the bond charge densities ρ_{\max} follow the trends $\rho_{\max}^{\text{Al-X}} \leq \rho_{\max}^{\text{Ga-X}} < \rho_{\max}^{\text{In-X}}$. Hence, among the sulfides, CuAlS₂ has the most ionic $A-X$ bond and the least ionic $B-X$ bond, whereas CuInS₂ has the least ionic $A-X$ bond but the most ionic $B-X$ bond. It is therefore not meaningful to ask "which of the CuBX_2 sulfides or selenides is the most ionic?" since the answer is different for each of the two bonds in the system. These trends agree remarkably well with the model bond ionicities calculated by Levine⁷¹ from the dielectric theory of ionicity, as well as with the observed trends in the nonlinear optical susceptibilities.⁷² Third, the sulfides have a larger bond polarity than the selenides both in the $A-X$ and in the $B-X$ contacts (i.e., $d_{\max}^{A-S} < d_{\max}^{A-Se}$ and $d_{\max}^{B-S} < d_{\max}^{B-Se}$). Fourth, whereas the $B-X$ bond charge is localized between two minima near the X and B sites, respectively, the $A-X$ bond charge is confined by a density minimum only near the anion site. The shaded areas in Figs. 16 and 17 highlight these different asymmetries be-

tween the two basic chemical bonds and suggest the higher stability of the Cu-X contact relative to the $B-X$ contact.

IX. ADJUSTING THE BAND STRUCTURE

As seen from Table V and discussed in the Introduction, the local-density formulation of interelectronic interactions²⁶ underestimates the optical band gaps relative to experiment. While many of the chemical trends in the electronic structure can be studied by using the local-density approach, investigation of the variations in the band gaps (e.g., with structural parameters) clearly requires that it will have a physically correct magnitude. This can be done in an *ad hoc* fashion by scaling the exchange coefficient²⁶ α . We find empirically that $\alpha = 1.0-1.1$ produces the correct optical gaps in these compounds. For example, Fig. 18 compares for CuInSe₂ the band structure obtained by using Ceperley's correlation²⁹ with the band structure obtained by using an exchange coefficient $\alpha = 1.1$. Table X compares the band energies in these two calculations. It is seen that upon scaling the exchange coefficient the $\text{Cu } d$ components of the upper valence band move to more negative energies relative to the original calculation, leading to an opening up of the optical band gaps due to the reduced $\Gamma_{15}(d)-\Gamma_{15}(p)$ repulsion (cf. Sec. III A). Scaling up the exchange coefficient increases the attractiveness of the crystal potential in regions of space of high charge density and therefore lowers the localized states (e.g., the $B^{III} d$ band and the $X^{VI} s$ band) more than the extended states (e.g., the upper valence band). This exercise clearly indicates

TABLE X. Comparison of the band structure of CuInSe₂ calculated with the Slater exchange (using $\alpha = 1.1$) and with the Ceperley exchange correlation^{27(c),29} (XC). Results (in eV) given relative to the $\Gamma_{4v}^{(2)}$ valence-band maximum. Results for Slater exchange with $\alpha = 1.0$ were given in Ref. 25.

State	Slater exchange	Ceperley XC	State	Slater exchange	Ceperley XC
Upper VB			$X^{VI} s$ band		
Maxima					
$\Gamma_{4v}^{(2)}$	0.0	0.0	$\Gamma_{5v}^{(1)}$	-13.03	-12.75
$\Gamma_{5v}^{(2)}$	-0.08	-0.03	Γ_{3v}	-13.06	-12.75
$T_{3v} + T_{4v}$	-0.79	-1.05	$\Gamma_{1v}^{(1)}$	-13.83	-14.00
$N_{1v}^{(5)}$	-0.54	-0.63	$T_{1v} + T_{2v}$	-13.00	-12.92
			$T_{5v}^{(1)}$	-13.46	-13.58
Minima					
$\Gamma_{4v}^{(1)}$	-5.15	-4.66	$N_{1v}^{(2)}$	-13.20	-12.96
$T_{4v} + T_{5v}$	-5.12	-4.61	$N_{1v}^{(1)}$	-13.31	-13.18
$N_{1v}^{(4)}$	-5.13	-5.02	$B^{III} d$ band	-21.48	-16.93
$B^{III}-X^{VI}$ band			Conduction bands		
$\Gamma_{1v}^{(2)}$	-5.14	-5.52	Γ_{1c}	0.98	-0.2
Γ_{2v}	-5.64	-6.32	Γ_{3c}	3.24	1.87
$T_{5v}^{(2)}$	-5.49	-6.15	Γ_{2c}	3.77	2.46
$N_{1v}^{(3)}$	-5.37	-6.17	$T_{1c} + T_{2c}$	2.76	1.64
			T_{5c}	3.60	1.95
			$N_{1c}^{(1)}$	2.25	1.39
			$N_{1c}^{(2)}$	4.83	3.37

that there does not exist a single exchange coefficient α that produces a correct optical gap *and* the correct energy positions of the localized bands. However, this empirical device of scaling up the exchange coefficient is adequate for the restricted scope of studying the variation of the band gap with structural parameters. Taking CuInSe₂ as an example, we find that although the band gap increases with exchange scaling ($E_g = -0.2$ eV using Ceperley's correlation and $E_g = 0.98$ eV using Slater's exchange $\alpha = 1.1$), its structural derivative dE_g/du is similar in both cases (18.2 and 21.1 eV for Ceperley's and Slater's functionals, respectively). This suggests that one can use a scaled exchange for the restricted objective of producing nonvanishing band gaps for the In compounds and studying their variations with structural parameters.³⁶ Details of such studies will be described in a forthcoming publica-

tion.⁷³ We conclude that despite the glaring failure of the density-functional formalism to produce correct band gaps, a judicious study of both scaled and unscaled results (cf. Table X) can provide physically meaningful bounds for the major chemical trends.

ACKNOWLEDGMENTS

The authors acknowledge useful and stimulating discussions with D. Cahen, S. Deb, J. Folmer, A. Hermann, and O. Jamjoun. One of us (J.E.J.) thanks P. Bendt for information on the computer routines and assistance in setting up the initial input data. This work was supported in part by the Office of Energy Research, Division of Materials Science, U. S. Department of Energy, Contract No. DE-AC02-77-CH00178.

- ¹E. Parthé, *Crystal Chemistry of Tetrahedral Structures* (Gordon and Breach, New York, 1964).
- ²N. A. Goryunova, *The Chemistry of Diamond-Like Semiconductors* (Chapman and Hall, New York, 1965).
- ³J. L. Shay and J. H. Wernick, *Ternary Chalcopyrite Semiconductors: Growth, Electronic Properties and Applications* (Pergamon, Oxford, 1974).
- ⁴U. Kaufmann and J. Schneider, in *Festkörperprobleme XIV* (Vieweg, Braunschweig, 1974), p. 229.
- ⁵S. Wagner, in *Electroluminescence*, edited by J. I. Pankove (Springer, Berlin, 1977), p. 171.
- ⁶A. MacKinnon, in *Festkörperprobleme XXI*, edited by J. Treusch (Vieweg, Dostmund, 1981), p. 149.
- ⁷A. Miller, A. MacKinnon, and D. Weaire, in *Solid State Physics*, edited by H. Ehrenreich, F. Seitz, and D. Turnbull (Academic, New York, 1981), Vol. 36.
- ⁸B. R. Pamplin, T. Kiyosawa, and K. Masumoto, *Prog. Cryst. Growth Charac.* **1**, 331 (1979).
- ⁹Deuxieme Conference Internationale sur les Composés Semiconductors Ternaires, Strasbourg, 1975 [*J. Phys. (Paris) Colloq.* **36**, C-3 (1975)].
- ¹⁰*Ternary Compounds 1977, Proceedings of the Edinburgh Conference on Ternary Compounds*, edited by G. D. Holah (Institute of Physics, Bristol, 1977).
- ¹¹Proceedings of the Fourth International Conference on Ternary and Multinary Compounds, Tokyo, Japan, 1980 [*Jpn. J. Appl. Phys.* **19**, Suppl. 19-3 (1980)].
- ¹²Proceedings of the Fifth International Conference on Ternary and Multinary Compounds, Cagliari, Italy, 1982 [*Nuovo Cimento* (in press)].
- ¹³S. Wagner, J. L. Shay, P. Migliorato, and H. M. Kasper, *Appl. Phys. Lett.* **25**, 434 (1974).
- ¹⁴L. L. Kazmerski and Y. J. Juang, *J. Vac. Sci. Technol.* **14**, 769 (1977).
- ¹⁵R. A. Mickelsen and W. S. Chen, in *Fifteenth IEEE Photovoltaic Specialists Conference 1981*, IEEE Publication No. 81CH1644-4 (unpublished), p. 800.
- ¹⁶N. Yamamoto, in Proceedings of the Fourth International Conference on Ternary and Multinary Compounds, Ref. 11, p. 45.
- ¹⁷J. E. Jaffe and A. Zunger (unpublished).
- ¹⁸M. L. Cohen and T. K. Bergstresser, *Phys. Rev.* **141**, 799 (1965).
- ¹⁹A. Zunger and M. L. Cohen, *Phys. Rev. B* **18**, 5449 (1978); **20**, 4082 (1979).
- ²⁰A. S. Poplavnoi and Yu. J. Polygalov, *Izv. Akad. Nauk SSSR, Neorg. Mater.* **7**, 1706 (1971); **7**, 1711 (1971) [*Inorg. Mater. (USSR)* **7**, 1527 (1971); **7**, 1531 (1971)].
- ²¹A. S. Poplavnoi, Yu. I. Polygalov, and A. M. Ratner, *Izv. Vyssh. Uchebn. Zaved. Fiz.* **6**, 7 (1976) [*Sov. Phys. J.* **19**, 689 (1976)].
- ²²W. A. Harrison, *Phys. Rev.* **131**, 2433 (1963).
- ²³T. Oguchi, T. Hamajima, T. Kambara, and K. J. Gondaira, in Proceedings of the Fourth International Conference on Ternary and Multinary Compounds, Ref. 11, p. 107.
- ²⁴A. Zunger and A. J. Freeman, *Phys. Rev. B* **15**, 4716 (1977).
- ²⁵P. Bendt and A. Zunger, *Phys. Rev. B* **26**, 3114 (1982).
- ²⁶W. Kohn and L. J. Sham, *Phys. Rev.* **140**, A1130 (1965).
- ²⁷(a) A. Zunger, J. Perdew, and G. Oliver, *Solid State Commun.* **34**, 933 (1980); (b) A. Zunger, *Phys. Rev. B* **21**, 4785 (1980); in *Structure and Bonding in Crystals*, edited by M. O'Keefe and A. Navrotsky (Academic, New York, 1981), p. 73; (c) J. P. Perdew and A. Zunger, *Phys. Rev. B* **23**, 5048 (1981).
- ²⁸W. Hanke and L. J. Sham, *Phys. Rev. B* **21**, 4656 (1980).
- ²⁹D. M. Ceperley and B. J. Alder, *Phys. Rev. Lett.* **45**, 566 (1980); D. M. Ceperley, *Phys. Rev. B* **18**, 3126 (1978). A convenient parametrization is given in Ref. 27.
- ³⁰P. Bendt and A. Zunger, *Bull. Am. Phys. Soc.* **27**, 248 (1982); Solar Energy Research Institute Report SERI/TP-212-1698 (unpublished); D. Wood and A. Zunger, *Bull. Am. Phys. Soc.* **28**, 386 (1983), and unpublished results.
- ³¹P. Löwdin, *J. Chem. Phys.* **19**, 1396 (1951).
- ³²M. L. Cohen, M. Schlüter, J. R. Chelikowsky, and S. G. Louie, *Phys. Rev. B* **12**, 5575 (1975); G. W. Pratt, *Phys. Rev.* **88**, 1217 (1982); L. G. Ferreira, *J. Comp. Phys.* **36**, 198 (1980); G. P. Kerker, *Phys. Rev. B* **23**, 3082 (1981); M. Manninen, R. Nieminen, and P. Hautojavi, *ibid.* **12**, 4012 (1975).
- ³³H. W. Spiess, U. Haeberlen, G. Brandt, A. Räuber, and J. Schneider, *Phys. Status Solidi B* **62**, 183 (1974).
- ³⁴D. J. Chadi and M. L. Cohen, *Phys. Rev. B* **8**, 5747 (1973); A. Baldereschi, *ibid.* **7**, 5212 (1973).
- ³⁵(a) E. Clementi and C. Roetti, *At. Data Nucl. Data Tables* **14**,

- 177 (1974); (b) W. Lotz, *J. Opt. Soc. Am.* **60**, 206 (1970).
- ³⁶J. E. Jaffe and A. Zunger, *Phys. Rev. B* **27**, 5176 (1983).
- ³⁷J. C. W. Folmer, Ph.D. thesis, University of Groningen, The Netherlands, 1981 (unpublished).
- ³⁸Y. Mirovsky, Ph.D. thesis, Weizmann Institute of Science, Rehovot, Israel, 1983 (unpublished); Y. Mirovsky and D. Cahen, *Appl. Phys. Lett.* **40**, 727 (1982).
- ³⁹J. L. Shay and H. M. Kasper, *Phys. Rev. Lett.* **29**, 1162 (1972).
- ⁴⁰S. Nagel, A. Baldereschi, and K. Maschke, *J. Phys. C* **12**, 1625 (1979).
- ⁴¹(a) G. Brandt, R. Rüber, and J. Schneider, *Solid State Commun.* **12**, 481 (1973); H. J. Von Bardeleben and R. D. Tomlinson, *J. Phys. C* **13**, L1097 (1980); (b) G. H. Chapman, J. Shewchun, J. J. Loferski, B. K. Garside, and R. Beaulieu, *Appl. Phys. Lett.* **34**, 735 (1979), (c) In nonstoichiometric CuInSe₂ Cu vacancies are readily formed. On the other hand, the calculated electronic charge densities imply that the Cu-X bond is stronger than the B-X bond. It is tempting to speculate that the Cu vacancy formation is accompanied by the exothermic relaxation of the four nearest Se dangling bonds, leading to an overall small formation energy for the relaxed Cu vacancy.
- ⁴²V. P. Gupta, V. K. Srivastava, and P. N. L. Gupta, *J. Phys. Chem. Solids* **42**, 1079 (1981).
- ⁴³M. J. Luciano and C. J. Vesely, *Appl. Phys. Lett.* **23**, 453 (1973).
- ⁴⁴J. C. Rife, R. N. Dexter, P. M. Bridenbaugh, and B. W. Veal, *Phys. Rev. B* **16**, 4491 (1977).
- ⁴⁵S. Kono and M. Okusawa, *J. Phys. Soc. Jpn.* **37**, 1301 (1974).
- ⁴⁶W. Braun, A. Goldmann, and M. Cardona, *Phys. Rev. B* **10**, 5069 (1974).
- ⁴⁷E. P. Domashevskaya, L. N. Marshakova, V. A. Terenkhov, A. N. Lukin, Ya. A. Ugai, V. I. Nefedov, and Ya. Y. Salyn, *Phys. Status Solidi B* **106**, 429 (1981).
- ⁴⁸W. Horig, H. Neumann, H. Sobotta, B. Schumann, and G. Kühn, *Thin Solid Films* **48**, 67 (1978).
- ⁴⁹E. Loschke, H. Neumann, R. D. Tomlinson, W. Horig, E. Eliot, N. Avgerinos, and L. Howarth, *Phys. Status Solidi A* **61**, K39 (1980).
- ⁵⁰C. Ricón, J. González, and G. Sanchez Perez, *Phys. Status Solidi B* **108**, K19 (1981).
- ⁵¹H. A. Weakliem and D. Redfield, *J. Appl. Phys.* **50**, 1491 (1979).
- ⁵²The authors are indebted to J. D. Meakin for a compilation of the references on the absorption coefficients.
- ⁵³S. M. Sze, *Physics of Semiconductor Devices* (Wiley Interscience, New York, 1969), p. 54.
- ⁵⁴A. Baldereschi and K. Maschke, in *Physics of Semiconductors 1978*, edited by B. L. H. Wilson (Institute of Physics, Bristol, 1978), p. 1167.
- ⁵⁵W. Horig, H. Neumann, H. J. Höbler, and G. Kühn, *Phys. Status Solidi B* **80**, K21 (1977); J. L. Shay, B. Tell, H. M. Kasper, and L. M. Schiavone, *Phys. Rev. B* **7**, 4485 (1973); W. J. Anderson, P. W. Yu, and Y. S. Park, *Opt. Commun.* **11**, 392 (1974).
- ⁵⁶P. Kistaiah, Y. Venudhar, K. S. Murthy, L. Iyengar, and K. V. K. Rao, *J. Phys. D* **14**, 1311 (1981).
- ⁵⁷A. Jayaraman, V. Narayanamurti, H. M. Kasper, M. A. Chin, and R. G. Maines, *Phys. Rev. B* **14**, 3516 (1976).
- ⁵⁸R. L. Hengehold and F. L. Pedrotti, *J. Appl. Phys.* **46**, 5202 (1975).
- ⁵⁹J. Ringeissen, J. L. Regolini, and S. Lewonczuk, *Surf. Sci.* **37**, 777 (1973).
- ⁶⁰J. L. Shay, in *Proceedings of the 11th International Conference on Physics of Semiconductors, Warsaw, 1972* (Elsevier, Amsterdam, 1972), p. 787; J. L. Shay, B. Tell, H. M. Kasper, and L. M. Schiavone, *Phys. Rev. B* **7**, 4485 (1973).
- ⁶¹J. Austinat, H. Nelkowski, and W. Schrittenlacher, *Solid State Commun.* **37**, 285 (1980).
- ⁶²M. J. Thwaites, R. D. Tomlinson, and M. J. Hampshire, *Solid State Commun.* **27**, 727 (1978).
- ⁶³W. Horig, H. Neumann, B. Schumann, and G. Kühn, *Physica Status Solidi B* **85**, K57 (1978).
- ⁶⁴J. Gan, J. Tauc, V. G. Lambrecht, Jr., and M. Robbins, *Solid State Commun.* **15**, 605 (1974); *Phys. Rev. B* **12**, 5797 (1975).
- ⁶⁵A. Miller, A. MacKinnon, and D. Weaire, in *Solid State Physics*, Ref. 7, p. 159.
- ⁶⁶A. Miller, A. MacKinnon, and D. Weaire, in *Solid State Physics*, Ref. 7, p. 165.
- ⁶⁷J. J. Polygalov, A. S. Poplavnoi, and A. M. Ratner, *J. Phys. (Paris) Colloq.* **36**, C3-129 (1975).
- ⁶⁸In Table VII of Ref. 25 the reciprocal-lattice vectors (3,1,3) and (2,1, $\frac{3}{2}$) were erroneously denoted as (3,7,3) and (2,3, $\frac{3}{2}$), respectively.
- ⁶⁹S. C. Abrahams and J. L. Bernstein, *J. Chem. Phys.* **59**, 5415 (1973); **61**, 1140 (1974).
- ⁷⁰A. Zunger, *Phys. Rev. B* **22**, 5839 (1980).
- ⁷¹B. F. Levine, *Phys. Rev. B* **7**, 2591 (1973).
- ⁷²B. F. Levine, *Phys. Rev. B* **7**, 2600 (1973).
- ⁷³J. E. Jaffe and A. Zunger (unpublished).